Reliability Engineering and System Safety 261 (2025) 111149

Contents lists available at ScienceDirect

Reliability Engineering and System Safety

journal homepage: www.elsevier.com/locate/ress

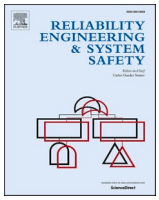

Optimal intensity measure and probabilistic seismic demand model for the assessment of historical masonry buildings: application to two case studies

Daniel Caicedo [a], Igor Tomić [b], Shaghayegh Karimzadeh [a,*], Vasco Bernardo [a,c], Katrin Beyer [b], Paulo B. Lourenço [a]

[a] University of Minho, ISISE, ARISE, Department of Civil Engineering, Guimarães, Portugal
[b] École Polytechnique Fédérale de Lausanne (EPFL), Earthquake Engineering and Structural Dynamics Laboratory (EESD), Lausanne, Switzerland
[c] Earthquake Engineering and Structural Dynamics Unit (Structures Department), National Laboratory for Civil Engineering (LNEC), Lisbon, Portugal

ARTICLE INFO

Keywords:
Probabilistic seismic demand model
Historical masonry buildings
Out-of-plane response
Lasso regression
Fragility curves

ABSTRACT

This paper presents a probabilistic seismic demand model (PSDM) as a relationship between intensity measures (IMs) and engineering demand parameters (EDPs) for the seismic assessment of two case studies resembling historical masonry buildings. The first one is representative of stiff monumental buildings, and the second of tall and slender masonry buildings. Both structures are modelled in the OpenSees software using three-dimensional macroelements that consider both the in-plane and out-of-plane response of masonry walls. A set of 100 accelerograms are selected to represent the seismic excitation. After full characterization of the seismic input in terms of IMs, both buildings are subjected to the action of these accelerograms to study the maximum structural response in the context of cloud analysis. The most suitable IMs are determined subsequently under the notions of efficiency, practicability, proficiency, and sufficiency. In addition, a composed measure is proposed as a linear combination in logarithmic space of the IMs that exhibit the best coefficient of determination (R^2) within the EDP vs. IM regression. This optimal composed measure is determined through machine learning-based Lasso regression. In the final stage of the study, fragility curves are derived to measure the likelihood of exceedance of certain levels of average roof displacement in terms of IM parameters.

1. Introduction

Performance-based earthquake engineering (PBEE) is the modern approach to seismic resistant design whose main outcome is the prediction of the performance of structures at different levels of damage state (DS) [1,2]. In this regard, PBEE seeks to determine fragility curves as the conditional probability of a structural system exceeding a DS, defined by a specific level of engineering demand parameter (EDP), at a given value of an intensity measure (IM) metric [3]. Applications of PBEE can be easily found, specifically oriented to reinforced concrete and steel frame building construction systems [4–6] or bridge structures [7,8]. Nevertheless, literature on PBEE of masonry structures is still limited, either for residential buildings or historical constructions as well as monuments.

Limitations in the available literature can be mainly attributed to two major factors. The first one is given by the extensive computational demand in large-scale modelling of masonry buildings [9,10], and the second is by the inherent uncertainties that make the realistic representation of masonry buildings a cumbersome task [11–14]. Despite this, remarkable efforts have been made to establish guidelines for seismic performance-based assessment of masonry structures [15]. Park et al. [16] proposed a structural modelling methodology to perform fragility analysis with an acceptable level of accuracy and without a significant increase in computational time. It was pointed out that the out-of-plane (OOP) stiffness of walls should be explicitly considered in the risk assessment of unreinforced masonry (URM) buildings. This is generally not done for the design or verification of new unreinforced and reinforced masonry buildings, as it is implicitly accounted for through simplified analysis methods [17–20]. Structural performance and fragility of heritage buildings was addressed using simplified models of masonry structures [21–24]. Battaglia et al. [25] considered the variability of structural and geometrical parameters in the seismic fragility assessment of masonry building aggregates, employing non-linear static analyses. A similar approach was adopted by Angiolilli et al. [26]. The seismic vulnerability of the masonry aggregate was assessed through nonlinear dynamic analysis and multiple stripe analysis. It was observed

* Corresponding author.
E-mail address: shaghkn@civil.uminho.pt (S. Karimzadeh).

https://doi.org/10.1016/j.ress.2025.111149
Received 29 December 2023; Received in revised form 11 April 2025; Accepted 12 April 2025
Available online 17 April 2025

that the damage limit state was mainly governed by the in-plane (IP) behaviour, while the collapse state by OOP mechanisms. On a similar context, a recent study by Tomić and Beyer [27] examined the prediction and postdiction of a shake-table test on a half-scale stone masonry aggregate tested by incremental bidirectional excitation. It was stressed out that simplified modelling of masonry aggregates can produce only seemingly satisfactory or conservative results. On top of that, Xu et al. [28] proposed a seismic-damage prediction method using machine-learning algorithms and a large catalogue of IMs (48 in total). The authors determined that, because of their complex dynamic features, URM buildings might require up to 13 IMs to achieve an accuracy level in the prediction higher than 90 %, in contrast with single-storey moment frames that require only one IM.

In a similar way, it is also worth mentioning some important works recently carried out and coordinated by the Italian Civil Protection Department (ICPD) on the definition of the seismic fragility of the Italian masonry building heritage. Rosti et al. [29] provided typological fragility curves, and fragility curves for vulnerability classes for residential unreinforced masonry buildings based on an empirical model calibrated on Italian post-earthquake damage data and compatible with the key features of the Italian national seismic risk platform [30]. Lagomarsino et al. [31] presented a heuristic macroseismic vulnerability model for unreinforced masonry existing buildings calibrated on the observed damage in Italy, as an extension of the original proposal of Lagomarsino and Giovinazzi in [32]. Porto et al. [33] validated the fragility models adopted by the ICDP for the assessment of national seismic risk by comparing predicted and observed damage scenarios and consequences on building stock (mainly residential masonry and reinforced concrete) and the population of the L'Aquila 2009 and Amatrice 2016 seismic events. Then, mechanics-based fragility curves were developed for Italian unreinforced masonry residential buildings [34] and schools [35] by classifying the structures according to a few parameters such as construction age, number of stories, plan area, and type of masonry (i.e. with regular or irregular pattern). More recently, Monti et al. [36] generated risk maps for Italy based on spectrum-consistent ag-based fragility that can be used at multiple locations and soils, preserving consistency is terms of spectral ordinates.

In recent years, probabilistic seismic demand analysis (PSDA) has become an important element of seismic fragility and risk analysis in the context of PBEE [37]. The main outcome of PSDA is better known as a probabilistic seismic demand model (PSDM), which denotes the probabilistic relationship between earthquake intensity and seismic demand. Such models are generally assumed to follow a power-law function within the median seismic demand vs. IM regression ($\eta_{EDP|IM}$), as stated by Cornell et al. [38]:

$$\eta_{\mathrm{EDP|IM}} = a\,\mathrm{IM}^{\,b} \tag{1}$$

with a and b as regression coefficients.

Nonetheless, other models, such as neural networks [39,40] or machine learning [41], can also study the relation between EDP and IMs. Early studies developed PSDMs for building structures [42,43], bridges [44,45], or concrete dams [46]. The seismic risk of alternative structural typologies has been approached using similar frameworks. For example, transmission tower-line systems subjected to mainshock-aftershock sequences [47,48]; steel diagrid systems [49]; nuclear power plants [50]; pile group-supported bridges [51]; open-pit slopes [52]; concrete face rockfill dams [53]; highway bridges [50]; electrical substations accounting for multi-stage uncertainties [54]; and more recently geo-structures using stochastic ground motion simulations [55]. In a similar context, Zhang et al. [56] addressed the reliability and failure probabilities of RC frame structures under progressive collapse due to different column-loss scenarios accounting for masonry infills through appropriate macro models. Zhou et al. [57] investigated the seismic risk of corroded RC frames with additional considerations of aftershock sequences leading to risk estimation 10 times higher than mainshock damage. The work by Vargas-Alzate et al. [58] identified high-efficiency IMs to predict the seismic response of building classes affected by near- and far-fault ground motion records. Furthermore, Guo et al. [59] proposed a general procedure to identify the optimal IMs, specifically for long span cable-stayed bridges, based on generalized linear regression models.

The objective of this study is twofold:

1. To develop PSDMs of two case study historical masonry buildings for the identification of optimal IMs under the notions of efficiency, practicability, proficiency, and sufficiency.
2. To adapt the Least absolute shrinkage and selection operator (Lasso) regression [60] to derive an optimal composed measure as a numerical parameter aimed at describing accurately the dynamic response of the masonry buildings in terms of specific EDPs.

The proposed methodology is applied to two case study buildings initially presented by Tomić et al. [11]. However, this framework may be extended to other building types. The first building (Holsteiner Hof) is representative of stiff monumental heritage structures, while the second (Lausanne Malley) is representative of tall and slender masonry buildings. The numerical models are developed in the OpenSees software [61] using a recently proposed three-dimensional macroelement to consider the IP and OOP response of masonry walls [62]. This results in an additional advantage compared to previous studies in which the activation of OOP failure modes is neglected [63] or assessed separately through kinematic limit analysis [64]. A large set of accelerograms is selected on the basis of unconditional selection [65], and the seismic input is fully characterised afterwards in terms of IMs. The response of the structural systems, considering the maximum average roof displacement and maximum base shear as EDPs, is examined in the cloud form. After the most suitable IMs are identified within PSDMs, Lasso regression methodology is adapted to compute the composed measure as a linear combination in logarithmic space of the IMs that exhibit the best coefficient of determination (R^2) within the EDP vs. IM regression. Finally, fragility curves are presented to measure the likelihood of exceedance of certain levels of average roof displacement in terms of IM parameters, considering the composed measure as well.

2. Case studies definition and numerical modelling

Two buildings located in different cities in Switzerland are selected as case studies [11]. Each building is representative of (i) stiff monumental heritage structures, and (ii) tall and slender residential masonry buildings. The following sub-sections present a brief description of the buildings' topology, modelling approach, adopted material and modelling parameters, assumption for the failure criteria and definition of EDPs.

2.1. Description of the buildings' topology

2.1.1. Holsteiner Hof

The Holsteiner Hof building, located in the city centre of Basel, is a 2-storey stone masonry building as depicted in Fig. 2a. The structure was built in 1752, following the architectural trend of the time. Thus, it is considered a landmark of cultural heritage, and it belongs to the Swiss Inventory of Cultural Property of National and Regional Significance. The building exhibits a regular rectangular plan with dimensions of 26.00 m × 14.00 m. The height of each storey is 4.50 m. Wall and spandrels thickness are 60 cm and 30 cm, respectively. The triangular gables at the top have a thickness of 45 cm. Thinner partitions, which are timber frame walls with brick infills ranging from 10 to 15 cm, can be found as part of the interior configuration. Nonetheless, their effect is neglected in the definition of the model since they are unlikely to influence the seismic response of the building in a significant manner. The floor system is composed of timber beams, simply supported on the walls

in the shorter direction, and a layer of planks nailed directly to the beams. In this sense, horizontal forces are transferred as friction forces from the beams to the walls. The roof structure is composed of a secondary truss system. Minor retrofitting interventions were reported during 1976–1979 that, in general, did not significantly modify the structural system.

2.1.2. Lausanne Malley

Different from the previous case study, this building is representative of tall and slender residential URM buildings. The building shown in Fig. 3a, is a 6-storey structure built during the second half of the 19th century and it is supported on reinforced concrete footings under the walls. The building is regular in plan with dimensions of 14.00 m × 12.00 m. The storey height varies between 2.90 − 3.20 m and the thickness decreases from 60 to 25 cm as the building grows in height. Thinner partition walls are present on the interior, but they are not accounted for in the numerical model. The floor system is composed of timber beams, simply supported on the walls in the shorter direction, and a layer of planks nailed directly to the beams. Thus, as with the Holsteiner Hof building, the horizontal forces are transferred as friction forces. The roof system is composed of a wooden truss structure. Soundproofing retrofitting measures were taken recently and reported in [66].

2.2. Modelling approach

The finite element method (FEM) [67,68] and the discrete element method (DEM) [69,70] denote the two main numerical methodologies to investigate the non-linear behaviour of masonry structures. Among them, the FE macro-modelling is a widely accepted strategy for the analysis of the global seismic response of masonry buildings through non-linear response history analysis (NLRHA). Both buildings are idealised through the equivalent frame model (EFM) approach in which façades are discretised into panel-scale components (i.e., piers and spandrels) commonly referred to as macroelements linked by rigid nodes in which damage is rarely observed [10,71]. Because of their simplicity, macroelements are usually implemented to assess the global response of masonry buildings through nonlinear dynamic analyses, accounting explicitly for different sources of modelling or input uncertainty. In this regard, the three-dimensional macroelement formulation introduced by Vanin et al. [62] for modelling the IP and OOP response of masonry walls is adopted in this research. The macroelement is implemented in the OpenSees software [61] and it is formulated as a one-dimensional element defined by two nodes at the element ends and one additional node at the midspan (See Fig. 1a). The macroelement is able to capture the IP and OOP response through three sectional models applied at the element ends and at the central section which can reproduce deformation across the main axes. OOP response is coupled with the IP response. P-Δ formulation is selected as geometric transformation in OpenSees to

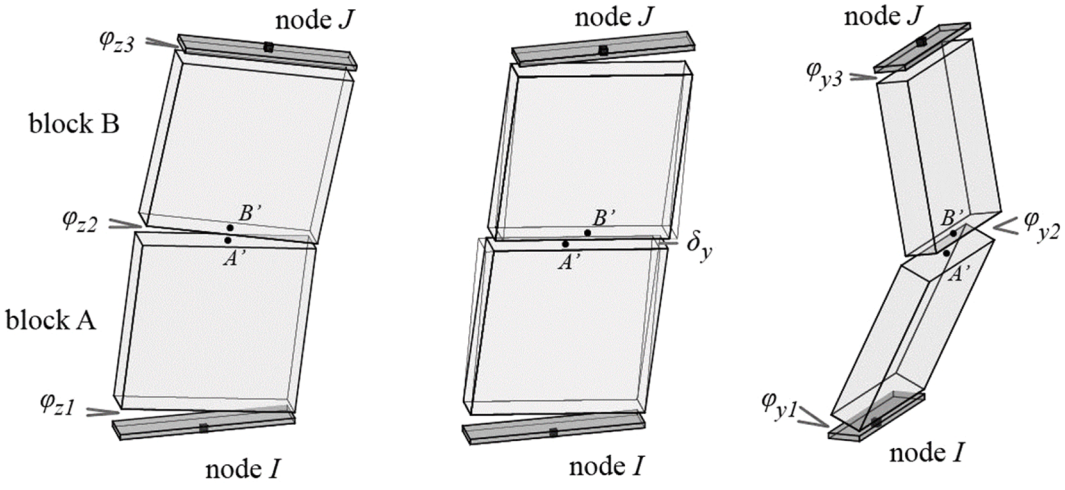

(a) Deformation modes of the macroelement (source Vanin et al. [62])

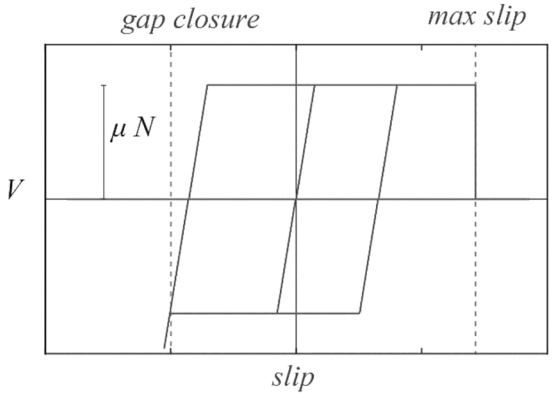

(b) Frictional constitutive law for floor-to-wall interfaces.

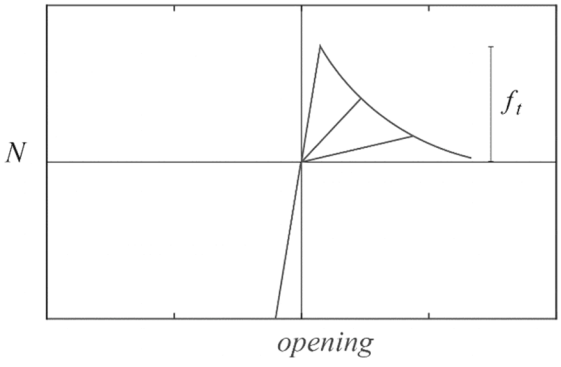

(c) Tension-damage constitutive law for wall-to-wall interlocking.

Fig. 1. General assumptions of the modelling approach. (a) Deformation modes of the macroelement (source Vanin et al. [62]). (b) Frictional constitutive law for floor-to-wall interfaces. (c) Tension-damage constitutive law for wall-to-wall interlocking.

capture second-order non-linear effects. Considering the rotations and lumped shear deformations at the central node, drift values can be calculated individually for flexural and shear deformations. Exceeding the limits in drift values, either $\delta_{c,flexure}$ or $\delta_{c,shear}$, can lead to the loss of lateral strength of the element. Such macroelements have been previously used for large-scale representation of masonry buildings [11,72,73].

Since the timber floors of both buildings are deformable, they cannot be idealized as rigid diaphragms. Thus, the floor system is modelled using orthotropic elastic membranes with higher stiffness in the direction of the beam span, and a lower stiffness in the remaining direction. The membrane definition is given by the two moduli of elasticity in the orthogonal directions, shear modulus, and thickness of the diaphragm (i.e., E_x, E_y, G_{xy}, and t_f, respectively). Although the floors are assumed as linear elastic, the floor-to-wall connections are modelled to account for non-linear behaviour and potential connection failure that can result in the OOP failure of a pier element (i.e., partial or total overturning of the façade [74]). To this aim, the floor nodes are modelled independently from the nodes defining the walls' geometry. Zero-length elements are used to model the frictional interfaces and possible relative displacement between the nodes. As shown in Fig. 1b, frictional sliding is allowed in the perpendicular direction to the wall while pounding of the beam towards the walls can occur in the opposite direction. Lastly, wall-to-wall interfaces are defined as zero-length elements following a uniaxial damage tension law with exponential softening and a linear elastic behaviour in compression (See Fig. 1c). This interface is used to simulate the formation of vertical cracks and separation of the orthogonal walls due to poor interlocking which can lead to the OOP failure of the macroelement.

2.3. Material and modelling parameters

In this study, the numerical model is assumed to be entirely deterministic. In other words, no source of uncertainty concerning masonry material and modelling parameters is accounted for in the analysis. Hence, the modelling parameters are assumed as the mean or median values reported in [11] (See Table 1). The properties for the definition of the elastic membrane are $E_x = 10.0 \times 10^9$ Pa; $E_y = 0.5 \times 10^9$ Pa; $G_{xy} = 10.0 \times 10^6$ Pa; and $t_f = 0.04$ m. Additional modelling parameters such as the pre-peak deformability in shear (G_c) [75], drift at 20 % force capacity loss, and residual friction coefficient (μ_R) are defined according to observations in the literature [75–78].

k_{floor}, f_w, and $\mu_{f\text{-}w}$, were implemented by Tomić et al. [11] to vary the values of the floor stiffness, stiffness of the interlocking interface, and the friction coefficient that governs the frictional sliding when accounting for material and modelling uncertainties. Nonetheless, the median value of 1 implies that their influence is neglected in this research since, as it was previously specified, no source of uncertainty concerning masonry material and modelling parameters is accounted for in the analysis. Additionally, all piers and spandrels were assigned the same material properties.

Table 1
Masonry and modelling parameters.

Parameter	Unit	Definition	Mean value
Masonry parameters			
E_m	[Pa]	Modulus of elasticity [76–78]	3.5×10^9
G_m	[Pa]	Shear modulus [76–78]	$1.5 \times 10^{9*}$
f'_{cm}	[Pa]	Compressive strength [76–78]	1.3×10^6
c_m	[Pa]	Cohesion [76–78]	$2.33 \times 10^{5*}$
μ_m	[-]	Friction coefficient [76–78]	0.25*
ρ	[kg]	Density [76–78]	2000
Modelling parameters			
k_{floor}	[-]	Floor stiffness factor [79,80]	1*
f_w	[-]	Wall-to-wall connection factor [81]	1*
$\mu_{f\text{-}w}$	[-]	Floor-to-wall friction coefficient [72,82]	1*
$\delta_{c,flexure}$	[-]	Drift capacity in flexure [83]	0.01035*
$\delta_{c,shear}$	[-]	Drift capacity in Shear [83]	0.007*
ζ	[-]	Damping ratio [72]	0.05

Note: (*) symbol over the values, denotes the median value taken from a lognormal distribution.

Figs. 2 and 3 depict the Holsteiner Hof and Lausanne Malley buildings, respectively, as well as the modal shapes of the numerical models developed in OpenSees using 3D macroelements. In both structures, the direction of the global x-axis coincides with the longitudinal direction of the main façade. For the Holsteiner Hof building, the periods computed for the first three vibration modes are 0.16 s, 0.14 s, and 0.12 s. The first two vibration modes in Fig. 2b and c, correspond almost entirely to translation in the two main axes, while the third mode, that is shown in Fig. 2d, answers to a more localised mechanism in which mainly the gables oscillate with some torsion at the upper corners. Now, for the Lausanne Malley building, the first three vibration periods correspond to 0.50 s, 0.42 s, and 0.33 s. Again, the first two modes depicted in Fig. 3b and c correspond to translation but are affected, this time, by the torsional effects that can be expected in the case of more tall and slender structures. Accordingly, the third one in Fig. 3d is mainly governed by a global torsional mode of the building. The results of modal analysis are consistent with the distribution of modal periods reported in [11], and the ambient vibration measurements of the second case study building, summarized in [66].

Lastly, for the nonlinear dynamic simulations, the Rayleigh model is assumed (proportional to mass and secant stiffness), calibrated at 5 % on the first and sixth frequencies for both buildings. Secant stiffness proportional damping model is adopted, in contrast to previous works [11,72] (which instead adopted initial-stiffness proportional damping), in order to avoid overdamping in the OOP mechanism, from the onset of the mechanism to failure.

2.4. Failure criterion and EDP definition

The failure criterion adopted in this research is similar to the one originally presented by Tomić et al. [11]. The global collapse/failure of the structure is reached either by (i) excessive OOP deformation of an element, thus, the $P-\Delta$ effect causes the loss of the global equilibrium, or (ii) triggered by a series of IP failures until the global equilibrium cannot be reached. The loss of equilibrium in a particular step of analysis triggers problems related to the numerical convergence and stability of the solution. Consequently, from this point the numerical solution is targeted as a failure, and the partial collapse induced by OOP local failure cannot be followed realistically. Alternative approaches, namely, discrete elements or applied element method might be a better fit for this purpose [84].

Subsequently, a failure characterisation routine is started to check the step of the analysis that had a loss of equilibrium. In the first place, OOP rotation around the middle node of the pier and relative displacement between two floors are considered. OOP failure is considered when relative top-bottom displacement is equal to the thickness of the element times an OOP limit factor, assumed as 1 in this research after Vanin et al. [62]. This process leads to the potential identification of two OOP mechanisms, which are central node overturning and partial overturning. If no OOP failure is encountered, the failure mode is classified as IP.

Regarding the IP failure, a macroelement can reach individually either the $\delta_{c,flexure}$ or $\delta_{c,shear}$ limit. After this point, its lateral stiffness and strength are set to zero, but it retains the ability to transfer axial load. When 50 % of the piers in the same direction of one storey reach their drift limits, the IP failure is triggered and labelled either as flexure or shear depending on the number of elements that reached the $\delta_{c,flexure}$ or $\delta_{c,shear}$ limit, respectively. This failure criterion routine was further modified to identify mixed IP failure, meaning that approximately the same number of piers exceeded the $\delta_{c,flexure}$ and $\delta_{c,shear}$ limits (refer to Section 2.3). Analogously, mixed IP-OOP failure locations can be also identified.

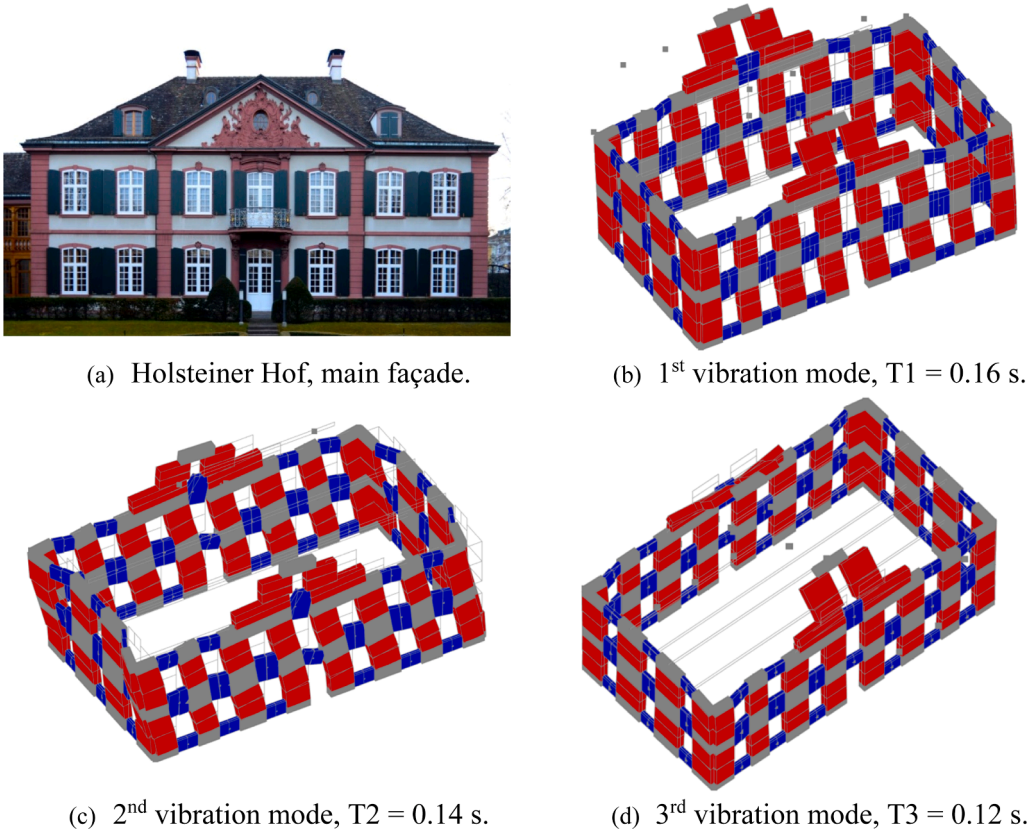

(a) Holsteiner Hof, main façade. (b) 1st vibration mode, T1 = 0.16 s.

(c) 2nd vibration mode, T2 = 0.14 s. (d) 3rd vibration mode, T3 = 0.12 s.

Fig. 2. Holsteiner Hof building and numerical model using 3D macroelements.

On the other hand, the selection of adequate EDPs is directly conditioned to the limitations of FE macroelement analysis. This modelling approach is mainly focused on the analysis of the global seismic response of masonry buildings since the *a priori* idealization of the structure in piers and spandrels usually leads to the definition of a mechanical system with limited representation of damage (e.g., inadequate prediction of realistic cracking patterns and complex failure mechanisms). Therefore, two global EDPs are selected to study the EDP vs. IM trend in the cloud response. These EDPs correspond to the maximum average roof displacement and maximum base shear (max($\overline{\Delta_r}$) and max(V_b), respectively). The selection of such EDPs is supported by investigations focused on the PSDA of building structures [11,58]. Hence, this study is limited to the analysis of the global response of the buildings in terms of max($\overline{\Delta_r}$) and max(V_b). The evolution of OOP failure mechanisms or partial collapse are not examined herein since the usage of macroelements to this end might lead to erroneous interpretations.

3. Ground motion selection and IM characterisation

A large set of accelerograms (n = 100) is selected on the basis of unconditional selection [65] (not dependent on structural periods). The records are selected from a large dataset of seismic records representative of some of the most relevant seismic-prone areas in Europe (i.e., Italy, Greece, Turkey, Portugal, etc.). The databases that are considered for this task include the reference database for seismic ground motion in Europe (RESORCE) [85], the pan-European engineering strong motion (ESM) [86], the Turkish accelerometric database provided by disaster and emergency management presidency (AFAD) [87], and the Italian accelerometric archive (ITACA) [88]. The seismological parameters for selection are set as: $4.5 \leq M_w \leq 7.8$; $90\ m/s \leq V_{s30} \leq 1050\ m/s$; $R_{JB} \leq 185$ km, covering, in this way, the widespread European hazard consistent with the collected dataset. Fig. 4 shows the 5 % damped geometric mean spectral acceleration (S_a) of the selected records, alongside the mean, median, and 95 % confidence interval.

The acceleration records are characterised in terms of their seismological parameters and IMs. The goodness of correlation between these metrics and the dynamic response of the masonry buildings in terms of EDPs will be assessed afterwards. A total of 84 metrics (larger than in similar studies conducted before [46,58,59]) are taken into account in this research. A classification similar to the one presented by Hariri-Ardebili and Saouma [46] is adopted to subdivide IMs into period and duration-related, ground motion dependent scalars; ground motion dependent compound, structure-independent spectral, and structure-dependent spectral IMs. Table 2 provides the definition and mathematical formulation for these metrics.

In Table 2, t_d is the total duration of a particular record. t_5, t_{75}, and t_{95} are the time values where the 5 %, 75 %, and 95 % of I_A are achieved, respectively. I_{A5-75}, which is needed for the computation of SIR, is given by the I_A within the interval t_5-t_{75}. Tm and Tp are indicators of frequency content. In this sense, C_i and f_i refer to the Fourier amplitudes of the entire accelerogram and the discrete Fourier transform frequencies in the range of 0.25–20 Hz needed for the computation of Tm. Tp simply refers to the period at which the maximum spectral acceleration occurs in an acceleration response spectrum calculated for 5 % viscous damping. On the other hand, u_g is the ground displacement, and the dots over u represent the derivatives of the function in time domain, denoting velocity and acceleration for one dot and two dots, respectively. S_a, S_v, and S_d represent spectral acceleration, velocity, and displacement, respectively. PSv is the pseudo-spectral velocity. ζ and T denote the damping ratio and period values within the spectra or pseudo-spectra. $T_P{}^a$ and $T_P{}^v$ are the periods where S_a and S_v reach the maximum values.

Regarding the structure-dependent IMs, the spectral acceleration, velocity, and displacement values are computed for the first 10 vibration modes of each structure. Additionally, values of spectral acceleration at fixed periods (i.e., T = 0.1, 0.2, 0.5, and 1.0 s) are also analysed. Cordova, S_a*, and Vamvatsikos, $\overline{S_a}$ or $\overline{\overline{S_a}}$, denote structure-dependant IMs

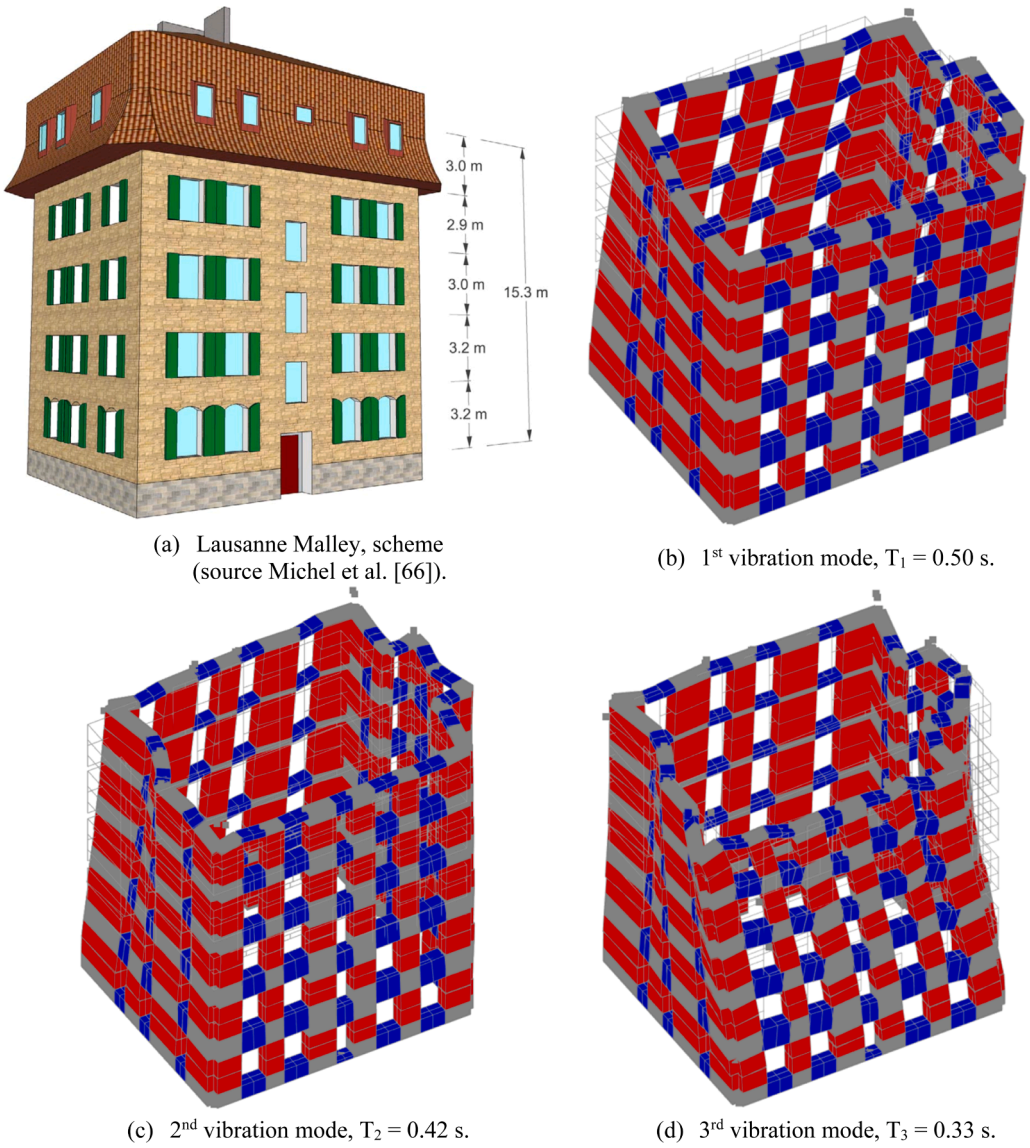

(a) Lausanne Malley, scheme (source Michel et al. [66]).

(b) 1st vibration mode, $T_1 = 0.50$ s.

(c) 2nd vibration mode, $T_2 = 0.42$ s.

(d) 3rd vibration mode, $T_3 = 0.33$ s.

Fig. 3. Lausanne Malley building and numerical model using 3D macroelements.

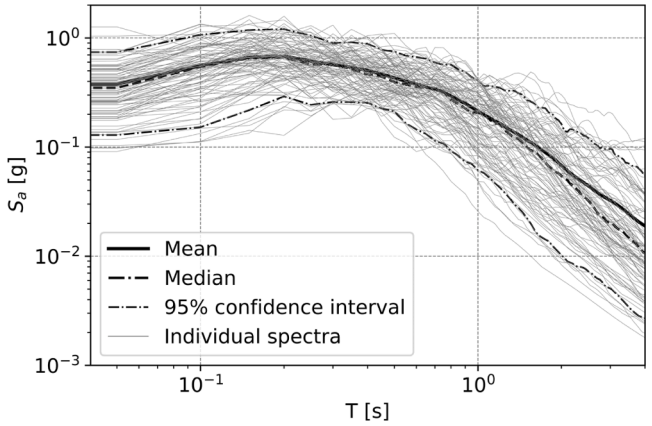

Fig. 4. 5 % damped geometric mean S_a of selected records.

that implicitly account for the inelastic behaviour by combining spectral acceleration ordinates at lengthened versions of the 1st mode of vibration, T_1. In this regard, the parameter c for the estimation of S_a^* is assumed as 2 based on Cordova et al. [104]. Similarly, T_a, T_b, and T_c are estimated as $T_a = T_1$; $T_b = 1.5T_1$, and $T_c = 2T_1$ after Vamvatsikos and Cornell [105]. Parameters α, β, and γ are derived by giving equal weights to the expressions $\alpha + \beta \leq 1$ or $\alpha + \beta + \gamma \leq 1$, as recommended in [104, 105]. Finally, α_i denotes the ratios of effective mass up to the N vibration mode of the structure [46,106]. $S_a{}^{1\text{-to-}N}$ is computed for combinations up to the 10th vibration mode for each case study building.

4. Probabilistic seismic demand models

This section provides a comprehensive discussion regarding the proposed framework for the development of a PSDM for the seismic assessment of historical masonry buildings, considering IP and OOP responses. The global regression models derived in this study seek to describe the behaviour of the system at different performance levels, from the linear range to yielding, up to collapse ultimately. The results of the seismic fragility assessment, derived directly from such PSDMs, are discussed independently in the next chapter. A brief theoretical background is provided alongside the criteria for optimal IM selection, and the basis for the derivation of a composed measure using Lasso regression. The discussion of the results is then presented for each case study building.

Table 2
IMs definition and mathematical formulation.

N°	Parameter	Definition	Mathematical formulation
Seismological parameters			
1	M_w	Moment magnitude	–
2	V_{s30}	Shear wave velocity	–
3	R_{epi}	Epicentral distance	–
4	R_{rup}	Rupture distance	–
5	R_{JB}	Joyner-Boore distance	–
6	R_{hyp}	Hypocentral distance	–
Period and duration-related IMs			
7	D_{5-75}	Significant (Arias) Duration [89]	$t_{75} - t_5$
8	D_{5-95}		$t_{95} - t_5$
9	Tm	Mean period [90]	$\frac{\sum_i C_i^2 \left(\frac{1}{f_i}\right)}{\sum_i C_i^2}$
10	Tp	Predominant period	$\max(S_a(\zeta = 0.05, T))$
Ground motion dependent scalars IMs			
11	PGA	Peak ground acceleration	$\max\left(\lvert \ddot{u}_g \rvert\right)$
12	PGV	Peak ground velocity	$\max\left(\lvert \dot{u}_g \rvert\right)$
13	PGD	Peak ground displacement	$\max\left(\lvert u_g \rvert\right)$
14	a_{RMS}	Root-mean-square of acceleration [91]	$\sqrt{\frac{1}{t_d}\int_0^{t_d} \ddot{u}_g^{\,2} dt}$
15	v_{RMS}	Root-mean-square of velocity	$\sqrt{\frac{1}{t_d}\int_0^{t_d} \dot{u}_g^{\,2} dt}$
16	u_{RMS}	Root-mean-square of displacement	$\sqrt{\frac{1}{t_d}\int_0^{t_d} u_g^{\,2} dt}$
17	I_A	Arias intensity [92]	$\frac{\pi}{2g}\int_0^{t_d} \ddot{u}_g\, 2dt$
18	CAV	Cumulative absolute velocity [93]	$\int_0^{t_d} \left\lvert \ddot{u}_g \right\rvert dt$
19	CAD	Cumulative Absolute Displacement	$\int_0^{t_d} \lvert \dot{u}_g \rvert dt$
20	SED	Specific energy density	$\int_0^{t_d} \dot{u}_g\, 2dt$
Ground motion dependent compound IMs			
21	PGV/PGA	Velocity to Acceleration Ratio	–
22	PGV^2/PGA		–
23	I_a	Riddell–Garcia intensity [94]	$PGA)(D_{5-95})^{1/3}$
24	I_v		$PGA)^{2/3}(D_{5-95})^{1/3}$
25	I_d		$(PGD)(D_{5-95})^{1/3}$
26	I_F	Fajfar intensity [95]	$(PGV)(D_{5-95})^{0.25}$
27	I_Z	Cosenza and Manfredi intensity [96]	$\int_0^{t_d} \ddot{u}_g^{\,2} dt/(PGA)(PGV)$
28	I_C	Characteristic intensity [97]	$(a_{RMS})^{1.5}(D_{5-95})^{0.5}$
29	SIR	Shaking intensity rate [98]	I_{A5-75}/D_{5-75}
Structure-independent spectral IMs			
30	EPA	Effective peak acceleration [99]	$\frac{1}{2.5}\int_{0.1}^{0.5} S_a(\zeta = 0.05, T) dT$
31	EPV	Effective peak Velocity [99]	$\frac{1}{2.5}\int_{0.8}^{1.2} S_v(\zeta = 0.05, T) dT$
32	IEPA	Improved effective peak acceleration [100]	$\frac{1}{2.5}\int_{T_p^a - 0.2}^{T_p^a + 0.2} S_a(\zeta = 0.05, T) dT$
33	IEPV	Improved effective peak velocity [100]	$\frac{1}{2.5}\int_{T_p^v - 0.2}^{T_p^v + 0.2} S_v(\zeta = 0.05, T) dT$
34	HI	Housner intensity [101]	$\int_{0.1}^{2.5} PS_v(\zeta = 0.05, T) dT$
35	ASI	Acceleration spectrum intensity [102]	$\int_{0.1}^{0.5} S_a(\zeta = 0.05, T) dT$

(*continued on next page*)

Table 2 (*continued*)

N°	Parameter	Definition	Mathematical formulation
36	ASI*	Modified acceleration spectrum intensity [103]	$\int_{0.1}^{2.0} S_a(\zeta=0.05,\mathrm{T})d\mathrm{T}$
37	VSI	Velocity spectrum intensity	$\int_{0.1}^{2.5} S_v(\zeta=0.05,\mathrm{T})d\mathrm{T}$
38	DSI	Displacement spectrum intensity	$\int_{2.0}^{5.0} S_d(\zeta=0.05,\mathrm{T})d\mathrm{T}$
Structure-dependent spectral IMs			
39–48	$S_a(\mathrm{T}_i)$	*Sa* at the i^{th} vibration mode	–
49–58	$S_v(\mathrm{T}_i)$	S_v at the i^{th} vibration mode	–
59–68	$S_d(\mathrm{T}_i)$	S_d at the i^{th} vibration mode	–
69	$S_a(T=0.1\ \mathrm{s})$	–	–
70	$S_a(T=0.2\ \mathrm{s})$	–	–
71	$S_a(T=0.5\ \mathrm{s})$	–	–
72	$S_a(T=1.0\ \mathrm{s})$	–	–
73	S_a^*	Cordova intensity [104]	$(S_a(\zeta=0.05,\mathrm{T}_1))^{\alpha}(S_a(\zeta=0.05,c\mathrm{T}_1))^{\beta}$
74	$\overline{S_a}$	Vamvatsikos intensity [105]	$(S_a(\zeta=0.05,\mathrm{T}_a))^{\alpha}(S_a(\zeta=0.05,c\mathrm{T}_b))^{\beta}$
75	$\overline{\overline{S_a}}$		$(S_a(\zeta=0.05,\mathrm{T}_a))^{\alpha}(S_a(\zeta=0.05,\mathrm{T}_b))^{\beta}(S_a(\zeta=0.05,\mathrm{T}_c))^{\gamma}$
76–84	$S_a^{1\text{-}to\text{-}N}$	Multiple period intensities [46,106]	$\prod_{i=1}^{N} S_a(\zeta=0.05,\mathrm{T}_i)^{\alpha_i}$

4.1. Brief theoretical background

Determining a PSDM is a crucial step within PBEE. PSDM states the conditional probability of an EDP reaching or exceeding a certain level of *edp*, given a seismic IM level, i.e., $P(\mathrm{EDP} \geq edp|\mathrm{IM})$. First of all, the results from multiple non-linear time history analyses should be determined to examine the EDP vs. IM cloud response. It is usually observed the $\eta_{\mathrm{EDP|IM}}$ follows a power-law distribution (linear in the logarithmic scale) as previously denoted in Eq. (1). Therefore, taking natural logarithm on both sides of Eq. (1) leads to:

$$\ln\left(\eta_{\mathrm{EDP|IM}}\right) = \ln a + b\ln\mathrm{IM} \tag{2}$$

Then, the logarithmic standard deviation (also called dispersion) approximates:

$$\beta_{\mathrm{EDP|IM}} \cong \sqrt{\frac{\sum_{i=1}^{n}\left(\ln edp_i - \ln\eta_{\mathrm{EDP|IM}}\right)^2}{n-2}} \tag{3}$$

Ultimately, it is assumed that the conditional seismic demand exhibits a lognormal distribution, thus, the results from cloud analysis can be aggregated to derive seismic fragility curves or PSDM defined by:

$$P(\mathrm{EDP} \geq edp\ |\mathrm{IM}) = 1 - \Phi\left(\frac{\ln edp - \ln\eta_{\mathrm{EDP|IM}}}{\beta_{\mathrm{EDP|IM}}}\right) \tag{4}$$

where Φ is the standard normal cumulative distribution function.

4.2. Optimal IM selection

An optimal IM can positively impact the accuracy of PSDM in estimating the seismic response of structural systems, such as historical masonry buildings in the context of this research. Commonly, notions of efficiency, practicability, proficiency, and sufficiency represent important metrics for the selection of optimal IMs [107–109]. Additional considerations such as correlation and hazard compatibility have also been accounted for in previous studies [46,52,53,59]. A brief explanation of these notions is provided next.

Efficiency: Efficient IMs exhibit lower variability or dispersion for the calculated seismic responses around the regression model [110]. Hence, efficiency is measured by the logarithmic standard deviation $\beta_{\mathrm{EDP|IM}}$. Lower values of $\beta_{\mathrm{EDP|IM}}$ denote highly efficient IMs.

Practicability: This notion denotes the dependency of the EDP against an IM metric. For linear regression models, as the one to be implemented herein, practicability can be estimated by the absolute value of the slope $|b|$ in Eq. (2). High $|b|$ values are indicators of increased practicability.

Proficiency: is a composed index of efficiency and practicability computed as:

$$\zeta = \frac{\beta_{\mathrm{EDP|IM}}}{|b|} \tag{5}$$

ζ is also referred to as modified dispersion which simplifies the optimal IM identification in terms of the highest practicability and lowest dispersion. Overall, lower ζ values indicate more proficient IMs.

Sufficiency: The notion of sufficiency implies the independence of the conditional probability distribution of EDP from seismological parameters such as $\mathrm{M_w}$ or distance metrics $\mathrm{R_{epi}}$, $\mathrm{R_{rup}}$, $\mathrm{R_{JB}}$, and $\mathrm{R_{hyp}}$. Sufficiency is calculated based on the *p*-values from linear regression of the residuals, $\epsilon^{\mathrm{EDP}}|\mathrm{IM}$. In general, significance levels greater than 5 % ($p > 0.05$) are considered to classify an IM parameter as sufficient.

Correlation: This criterion reflects the goodness of fit of the empirical regression model. The R^2 parameter is adopted to determine the goodness of fit. Higher values of R^2, closer to 1, imply larger accuracy in the prediction of the data trend and less scatter in the regression model.

Regarding hazard compatibility, it corresponds to the level of computational requirement in the estimation of hazard curves for a particular IM [110]. Nonetheless, the concept is ignored in this investigation not only because of the great advances in processing power during the last years but also because of the great potential of ground motion models recently proposed [111,112].

4.3. Procedure to find an optimal composed measure

Especially for the case of very complex structures, as can be the case of masonry buildings, whose dynamic behaviour is influenced by multiple sources of non-linearity (i.e., materials, second-order effects, floor-to-wall, and wall-to-wall connections, etc.) only one IM is not likely to provide good predictions for the dynamic response in terms of EDPs [28]. For this purpose, a composed measure (I_{comp}) is proposed as a linear combination in the logarithmic space of the IMs that exhibit the best R^2 within the EDP vs. IM regression. Lasso regression [60] is adapted to identify the necessary IMs, and then derive the optimal I_{comp} that best describes the dynamic response of the masonry buildings in terms of EDPs. Lasso regression was implemented in the context of

PSDMs by Guo et al. [59]. In this study, six IMs were identified as the optimal ones for a cable-stayed bridge, which combinedly led to one single numerical IM that significantly increased the fitting ability of the regression model. Nonetheless, the methodology proposed herein is different from the one presented by Guo et al. [59] and it is based on Lasso regression's ability to perform variable selection and regularization to prevent overfitting and enhance the accuracy of statistical models.

In this regard, the objective function to minimize in the Lasso regression is mathematically defined as:

$$f(\theta) = \sum_{i=1}^{n} \left(y_i - \sum_{j=1}^{m} x_{ij}^{T} \theta_j \right)^2 + \lambda \sum_{j=1}^{m} |\theta_j| \tag{6}$$

where $\boldsymbol{\theta} = [\theta_1, \theta_2, \ldots, \theta_m]^T$ is the regression coefficient vector with size m denoting the amount of input variables or IMs in this context; $\boldsymbol{x}_i = [x_{i,1}, x_{i,2}, \ldots, x_{i,m}]^T$ is the i^{th} input variable vector out of the n analyses (n = 100, as established in Section 3); accordingly, y_i is the i^{th} observed response (i.e., value of EDP obtained from time history analyses); and λ is the hyperparameter used for regularization that controls the strength of the penalty applied to the model coefficients. As λ increases, the more the coefficients for regression are shrunk toward zero. Note that the first term at the right side of Eq. (6) represents an ordinary least square problem, while the term $\lambda \sum_{j=1}^{m} |\theta_j|$ is the additional penalty to the objective function. This penalty based on the absolute value of the regression coefficients, will force some of these coefficients to become zero, meaning that the lasso procedure encourages simple models with fewer parameters. Hence, the I_{comp} can be founded as:

$$I_{comp} = \prod_{j=1}^{m} \mathrm{IM}_j^{\theta_j} \tag{7}$$

where the m relevant IMs for the structure under analysis are recognised as those that exhibit the best correlation within the EDP vs. IM regression ($R^2 \geq 0.6$ is assumed in this research as an acceptable level of correlation). I_{comp} has the potential to enhance the EDP-IM correlation at a relatively low cost since, in general, the process for its computation is simple and straightforward. Yet, this metric does not have a clear unit for its measure since it is no longer a physical parameter but rather a numerical structure-specific parameter. A Python routine was programmed using the LassoCV class from the scikit-learn library. The parameter cv is set as 10, thus, 10-fold cross-validation is implemented to automatically find the best λ that minimizes cross-validation error [113].

4.4. Discussion of results

4.4.1. Holsteiner Hof

Out of the 100 non-linear dynamic analyses conducted for the Holsteiner Hof building, 9 failed with an approximate even distribution between OOP and IP mechanisms (56 % and 44 %, respectively). For the case of IP failure observations, in 75 % of the cases, most of the pier elements exceeded the $\delta_{c,shear}$, leading to shear IP failure, while the rest of the observations corresponded to flexure IP failure. No mixed IP failure was observed in this case. In addition, approximately 50 % of the IP failures are observed on floor 1 in the "y" direction (F1 y-dir) while the rest are evenly distributed between floor 2 in the "x" direction, and floor 3 in the "x" direction (F2 x-dir and F3 x-dir, respectively). Similarly, for the OOP failure observations, 60 % of them are detected in F1 y-dir, while the remaining 40 % of OOP failures are distributed between F1 x-dir and F2 x-dir. Further, all OOP failure observations correspond to overturning around the central node. It is worth to emphasise that these statistics correspond to just a small sample of failure observations, i.e., 4 cases for IP and 5 OOP. Hence, such statistics do not represent conclusive evidence to characterise the behaviour at the collapse stage. Other methodologies, such as incremental dynamic analyses (IDA) [114]or multiple stripe analyses (MSA) [115], can be used for that purpose, which is not the aim of this research. A full characterization of the collapse mechanism for the Holsteiner Hof building through IDA, supporting the reliability of the 3D macroelement modelling approach, was recently addressed in [116]. A more comprehensive interpretation of these results can be achieved by means of the statistics depicted in Fig. 5.

Results of cloud analysis are presented in Fig. 6(a) and (b) considering the EDPs as the maximum average roof displacement and maximum base shear (max($\overline{\Delta_r}$) and max(V_b), respectively. Out of all analyses, the maximum values of EDP obtained were max($\overline{\Delta_r}$) = 35.39 mm, and max(V_b) = 3723 kN. Thus, asymptotic values of 40 mm and 4000 kN were set to denote the collapse DS for the max($\overline{\Delta_r}$) and the max (V_b), respectively. These values correspond to the critical ones before collapse, defined by the failure criterion previously exposed [11], or simply by problems with numerical convergence and stability of the solution. A higher level of scatter is observed in Fig. 6(a) when max($\overline{\Delta_r}$) is assumed as EDP.

Table A1 in the appendix reports the values for the assessment of the 84 IMs considered in this study, based on the criteria previously exposed in Section 4.2. IMs with R^2 greater than or equal to 0.6, in at least one of the two EDPs, are marked in bold. These marked IMs correspond to PGA, EPA, IEPA, ASI, S_a*, $\overline{S_a}$, and $\overline{\overline{S_a}}$. In all cases, the R^2 value is greater when the dynamic behaviour is described in terms of max(V_b) rather than max ($\overline{\Delta_r}$). Such observations are expected based on the scatter shown in Fig. 6 for both EDPs. This behaviour is also coherent with the values of logarithmic standard deviation, $\beta_{\text{EDP|IM}}$, which are always smaller when considering max(V_b) as EDP. Similarly, the values of modified dispersion, ζ, also confirm this hypothesis. Regarding practicability, in general, all 7 preselected IMs exhibit the highest $|b|$ values of all IMs evaluated in Table A1, being the slope always larger for the case of max ($\overline{\Delta_r}$). In terms of sufficiency, the seven IMs show p-values larger than 0.05 indicating the sufficiency of the group. In particular, among the 7 preselected IMs, PGA exhibits the lowest p-values, which are coherent with the findings of past investigations where it has been demonstrated that PGA predictions are closely related with distance metrics [112, 117–119]. It is also worth noting that all seven preselected IMs are acceleration-related metrics. This can be associated with the behaviour of short-period structures which are more sensitive to acceleration [120]. Outstanding predictions are observed for the dynamic response of the building, and regardless of the EDP, using S_a*, $\overline{S_a}$, and $\overline{\overline{S_a}}$. This might be interpreted since these particular measures account for structural damage and period lengthening, which is clearly observed after the action of the seismic input through non-linear dynamic analyses. In this regard, Fig. 7 shows the PSDM for the individual IMs with $R^2 \geq 0.60$, excluding failure cases from the regression. These regression models follow the power-law form described in Eq. (1) that becomes linear in the logarithmic space after the transformation in Eq. (2). Other investigations have adopted different assumptions for the prediction of the seismic demand, such as polynomial regression, either quadratic [58] or cubic [59], or even non-parametric predictive models based on artificial neural networks [39,40] to avoid the bias induced by closed-form expressions. However, this research sticks to the power-law approach in which the distribution of the seismic demand is assumed to be lognormal, useful for the subsequent derivation of I_{comp} and associated fragility functions. In future research, machine-learning models will be adopted to predict the seismic demand distribution of historical masonry constructions similar to [121,122].

The effect of dispersion is clear for each plot depicted in Fig. 7, especially with the max($\overline{\Delta_r}$) as EDP. Thus, although an acceptable fitting is achieved, reflected by the R^2 values, PSDMs based on only one IM are not adequate enough to provide good predictions for the dynamic response of the building in terms of the selected EDPs. In this regard, the machine learning approach based on Lasso regression is now adapted to

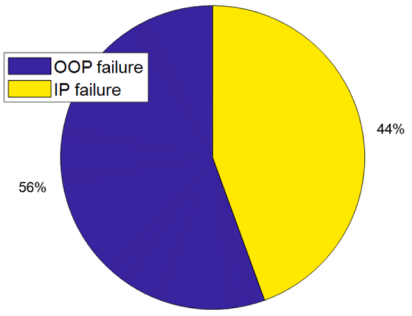

(a) IP and OOP failure distribution

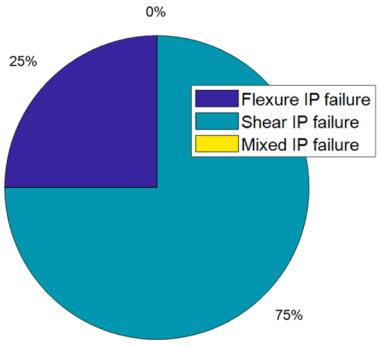

(b) Shear, flexure, and mixed observation for IP failure

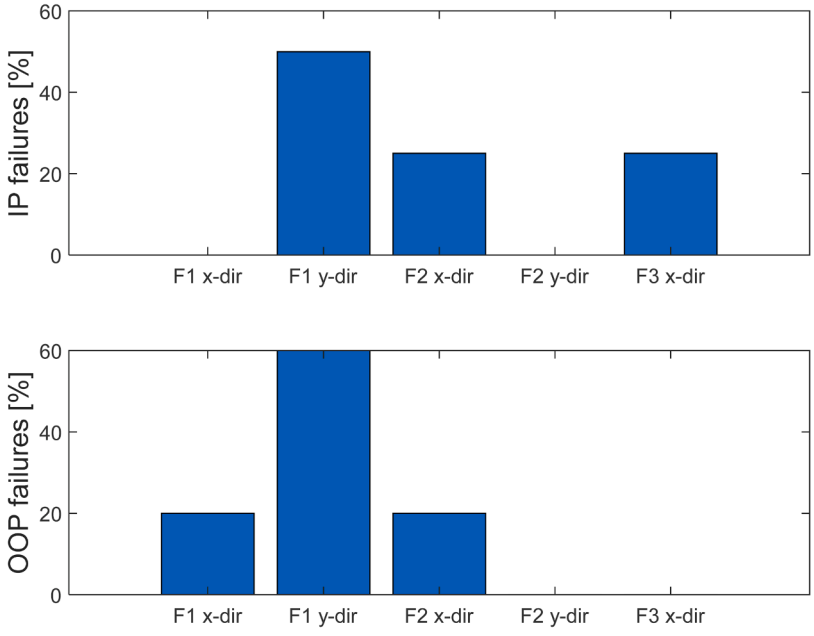

(c) IP and OOP failure localization

Fig. 5. Failure statistics — Holsteiner Hof building.

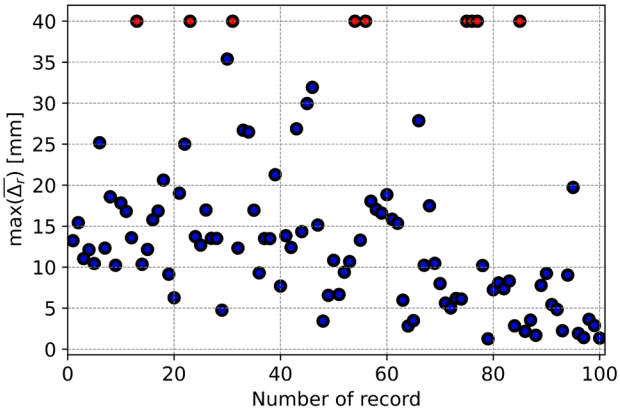

(a) $\max(\overline{\Delta}_r)$

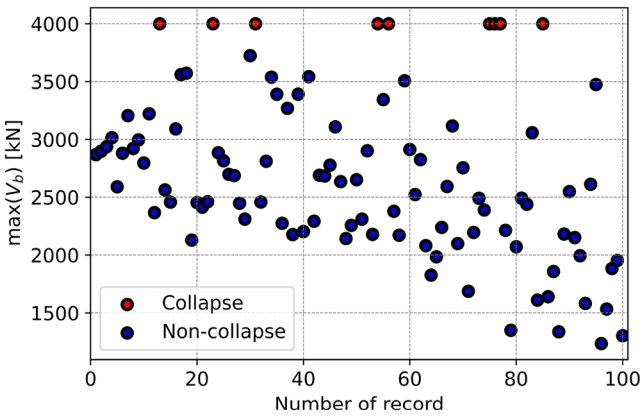

(b) $\max(V_b)$

Fig. 6. Results of cloud analyses — Holsteiner Hof building.

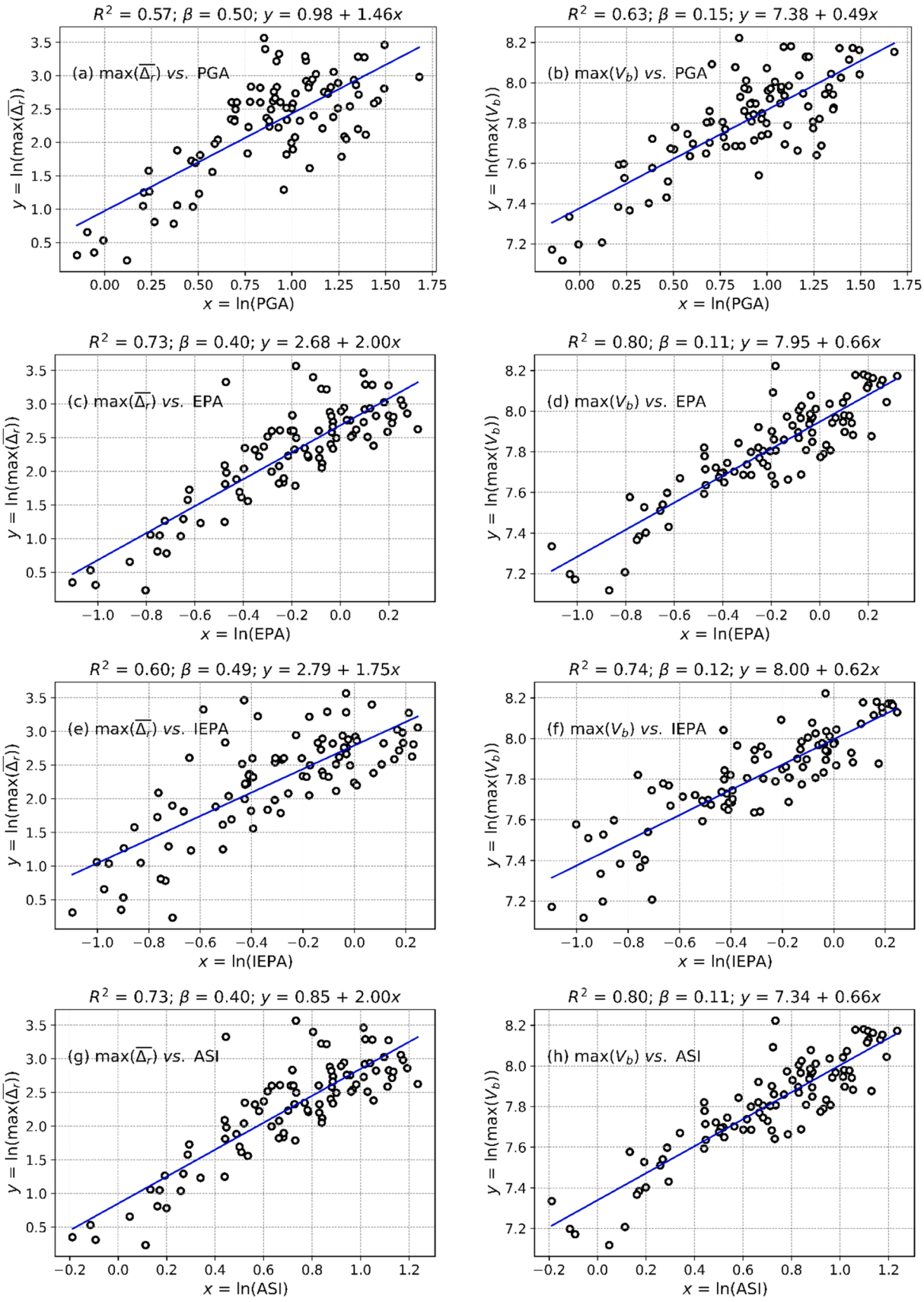

Fig. 7. PSDM for individual IMs — Holsteiner Hof building.

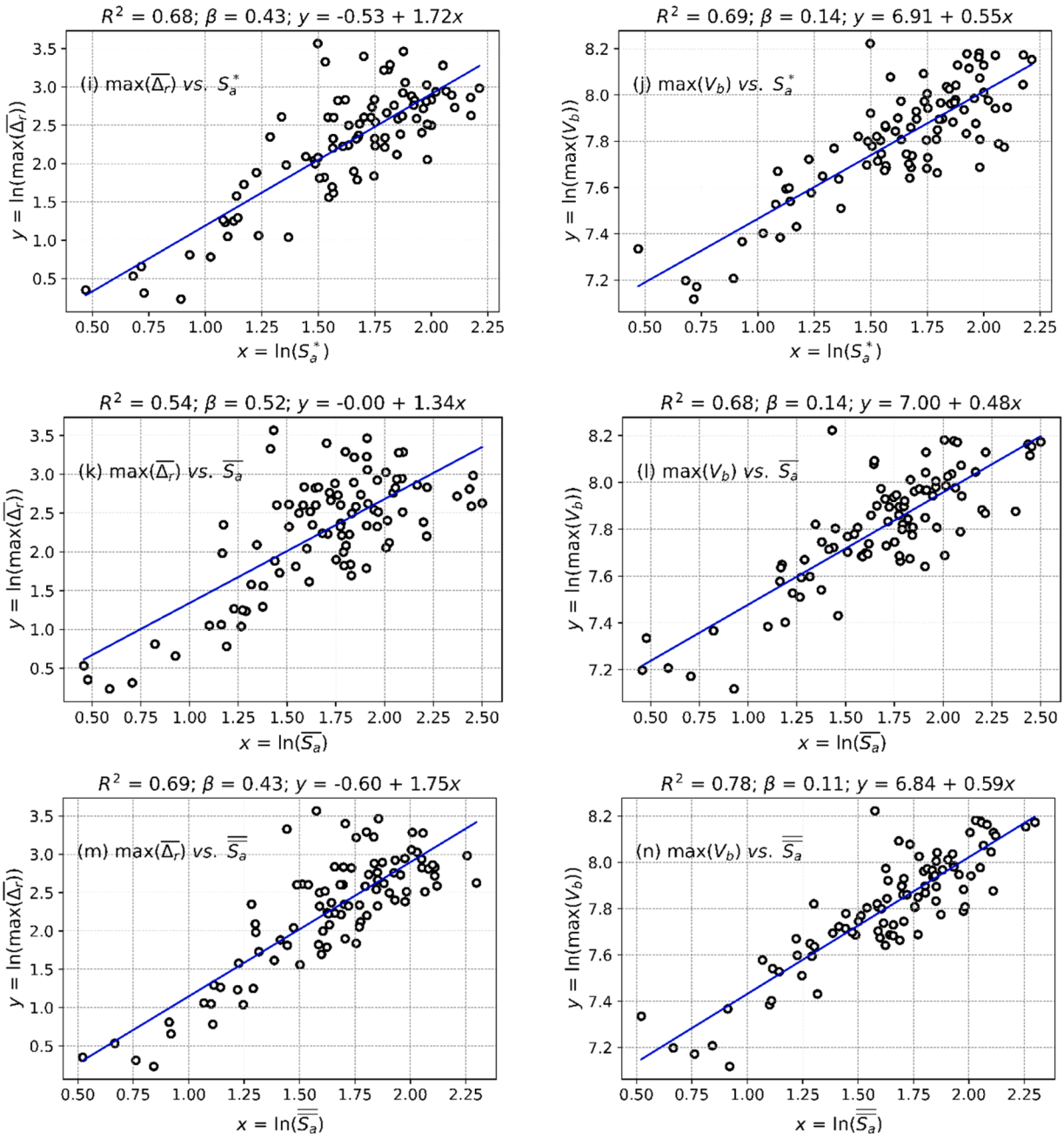

Fig. 7. (*continued*).

provide more accurate PSDMs for both max($\overline{\Delta_r}$) and max(V_b). I_{comp} can be interpreted as the integration of the preselected IMs using the criteria $R^2 \geq 0.6$. Thus, I_{comp} is directly related to the performance of the structure under analysis. The procedure for the computation of I_{comp} was described thoroughly in the previous section of the manuscript. Table 3 summarizes the regression coefficients, θ_i, associated with each of the preselected IMs for both EDPs. Fig. 8 shows the PSDMs by using I_{comp} as the independent variable. $I_{comp}{}^{(1)}$ and $I_{comp}{}^{(2)}$ in the "x" axis of each subplot corresponds to its computation after using the first or second combination of θ_i reported in Table 3, since I_{comp} is calculated separately for the two EDPs under analysis (i.e., max($\overline{\Delta_r}$) and max(V_b), respectively).

Table 3
Regression coefficients — Holsteiner Hof building.

EDP	Regression coefficients θ_i						
	PGA	EPA	IEPA	ASI	S_a^*	$\overline{S_a}$	$\overline{\overline{S_a}}$
max($\overline{\Delta_r}$)	0.48	1.16	−0.13	0.16	0.07	−1.38	1.69
max(V_b)	0.06	0.15	0.23	0.00	0.00	0.00	0.21

A considerable improvement is observed for both PSDMs in terms of R^2 values and dispersion, especially for the case of max($\overline{\Delta_r}$) in which R^2 increased up to 0.77 and dispersion reduced up to 0.37. The best values within the max($\overline{\Delta_r}$) regression using single IM were $R^2 = 0.73$ and $\beta = 0.40$, either with EPA or ASI. However, for the case of the max(V_b) vs. I_{comp} regression, the improvement was marginal, being the results comparable to the ones obtained through EPA or ASI individually. Another important thing to stress is that, regardless of the EDP adopted in the PSDM, the slope b in the regression model will always tend to 1 because of the mathematical formulation proposed for I_{comp} (See Eq. (7)). Thus, the practicability of I_{comp} is unconditional and invariant. It is observed how some of the coefficients, specifically for max(V_b) as EDP,

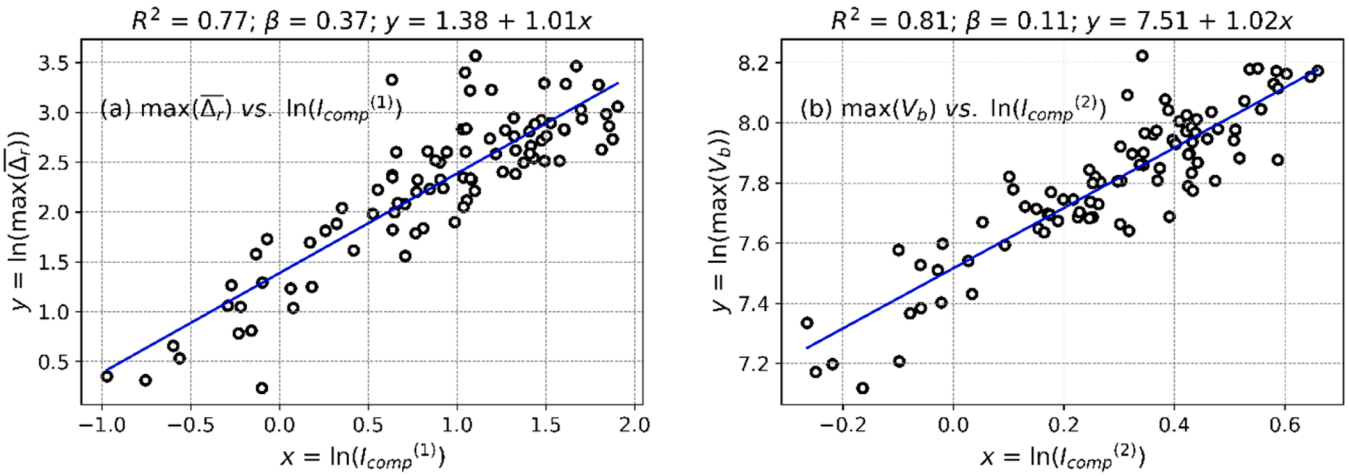

Fig. 8. PSDM with I_{comp} as independent variable using LASSO regression — Holsteiner Hof building.

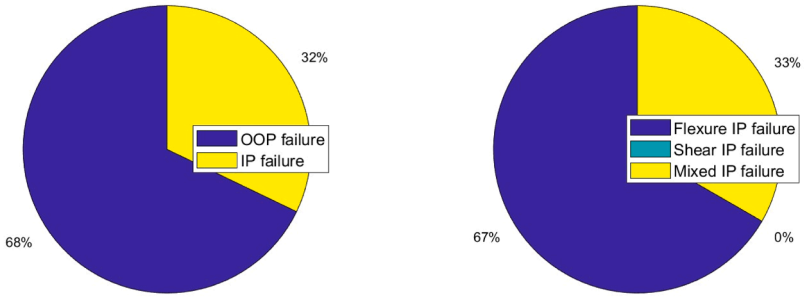

(a) IP and OOP failure distribution

(b) Shear, flexure, and mixed observation for IP failure

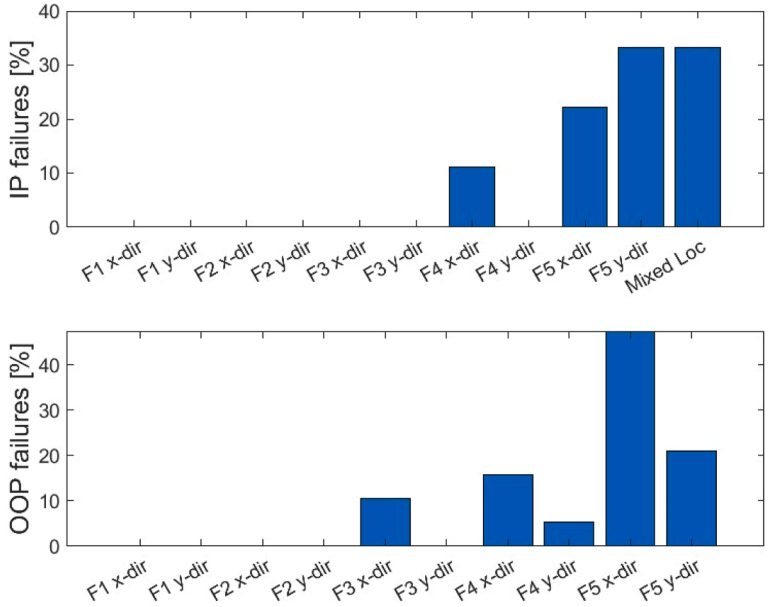

(c) IP and OOP failure localization

Fig. 9. Failure statistics — Lausanne Malley building.

drop to zero after minimization, which demonstrates the capability of Lasso regression to derive simple and accurate models with fewer variables.

4.4.2. Lausanne Malley

On this occasion 28 out of the 100 conducted non-linear dynamic analyses failed, 32 % of the time IP and 68 % OOP. Regarding IP failures, 67 % of the observations corresponded to flexure failure while the rest of them were classified as mixed IP. Moreover, all IP failures are observed at the upper storeys with >50 % concentrated at the last top-storey level, either F5 x-dir or F5 y-dir. Around 10 % and 30 % were observed at F4 x-dir and mixed locations, respectively. Similarly, OOP failures are also detected at upper stories with almost 50 % of the occurrences concentrated at F5 x-dir and the others evenly distributed among F3 x-dir, F4 x-dir, F4 y-dir, and F5 y-dir. Regardless of the small portion of collapse cases, the observation of failure mainly at upper stories is consistent with previous findings in the literature [116,123] supporting the validation of the modelling approach. All the collapse information is summarized in Fig. 9. In addition, the cloud response of the analyses is presented in Fig. 10. The maximum computed EDPs corresponded to $\max(\overline{\Delta_r}) = 42.26$ mm, and $\max(V_b) = 4971$ kN. Consequently, collapse is denoted by asymptotic values of 45 mm and 5000 kN for the $\max(\overline{\Delta_r})$ and the $\max(V_b)$, respectively.

The values for the assessment of IMs in terms of efficiency, practicability, proficiency, sufficiency, and correlation are reported in Table A2. As with the Holsteiner Hof building, the same criterion is adopted to preselect the best IMs (i.e., correlation greater than or equal to 0.6). The pre-selected IMs correspond, in this case, to PGV, ASI*, VSI, $S_a(T_1)$, $S_v(T_1)$, $S_d(T_1)$, S_a*, $\overline{S_a}$, and $\overline{\overline{S_a}}$. In terms of practicability, the slope b is always greater when the preselected IMs are implemented to describe the dynamic behaviour of the building in terms of $\max(\overline{\Delta_r})$ rather than $\max(V_b)$. Although the measurement of efficiency seems to be better for the global $\max(V_b)$, the values of modified dispersion, ζ, favour the response in terms of $\max(\overline{\Delta_r})$ with a mean value in the order of 0.30; while for the $\max(V_b)$ the values of ζ oscillate around a mean value of 0.42. In general, most the IMs under analysis exhibit p-values larger than 0.05 implying the sufficiency of the group. Different than for the first case study building, the 9 pre-selected measure do not correspond directly to acceleration-related metrics. On this occasion, the analysis also pointed out some velocity and even displacement-related IMs, such as PGV, VSI, $S_v(T_1)$, and $S_d(T_1)$. These observations are in agreement with the findings of [28] indicating that complex structures such as URM buildings require a large number of IMs to achieve acceptable predictions in their dynamic performance. Further, previous investigations have linked the sensitivity of OOP failures, which are largely observed for the Lausanne Malley building (19 out of 28 collapse cases), to velocity-related metrics [124]. Overall, the best predictions were achieved by means of $S_a(T_1)$. $S_v(T_1)$, $S_d(T_1)$, and $\overline{S_a}$, accounting this last one for structural damage and period lengthening. Fig. 11 shows the PSDM for Lausanne Malley building considering individual IMs with $R^2 \geq 0.60$.

Again, a linear trend is clearly observed within the regression models depicted in Fig. 11 which validates the assumptions of the power-law model mathematically described in Eq. (1). Among them, the best regression models relate to $S_a(T_1)$ and $S_d(T_1)$ for the $\max(\overline{\Delta_r})$, and PGV for the $\max(V_b)$, exhibiting R^2 values of 0.75 and 0.66, respectively. Now, the methodology proposed in Section 4.3 is applied to derive a composed measure able to predict the dynamic behaviour of the building with better accuracy. Fig. 12 portrays the PSDMs derived after I_{comp} for both global EDPs under analysis. As in the previous section, $I_{comp}{}^{(1)}$ and $I_{comp}{}^{(2)}$ correspond to the combination of the regression coefficients, θ_i, for the $\max(\overline{\Delta_r})$ and $\max(V_b)$ models, respectively. Table 4 summarizes the regression coefficients, θ_i, associated with each of the 9 preselected IMs for both EDPs. The correlation values obtained from the LASSO regression correspond to $R^2 = 0.84$ for the $\max(\overline{\Delta_r})$ and $R^2 = 0.77$ for the $\max(V_b)$, indicating a considerable enhancement against PSDM with single IMs. Dispersion was also improved, reducing the values to 0.21 and 0.12 for the $\max(\overline{\Delta_r})$ and $\max(V_b)$, respectively. As in the previous case, the slope b within the regression model tend to the unit value leading to $\zeta = \beta_{EDP|IM}$ (i.e., proficiency nearly identical to efficiency). Overall, the proposed I_{comp} stands as an optimal measure for the analysis of the dynamic response of masonry buildings offering clear enhancements in terms of correlation, efficiency, practicability, and proficiency. The effect of I_{comp} in the seismic fragility analysis of masonry structures is addressed in the next section.

5. Seismic fragility analysis

The final part of this study focuses on the presentation and discussion of PSDM-based fragility curves obtained after the aggregation of the results from cloud analysis. Fragility curves are a key component of risk assessment; they provide a probabilistic measure of vulnerability to hazards, which is essential for estimating potential losses and guiding risk mitigation strategies. In the context of PBEE and risk assessment, fragility curves for building structures are commonly associated with the probability of exceedance of diverse levels of displacement-related metrics rather than base shear [42,43]. Furthermore, roof displacement represents a familiar measure to most practitioners and researchers in the field of civil and structural engineering. Therefore, the $\max(\overline{\Delta_r})$ is selected as EDP to show the likelihood of exceedance of certain levels of DS in terms of the optimal individual IMs and the I_{comp}

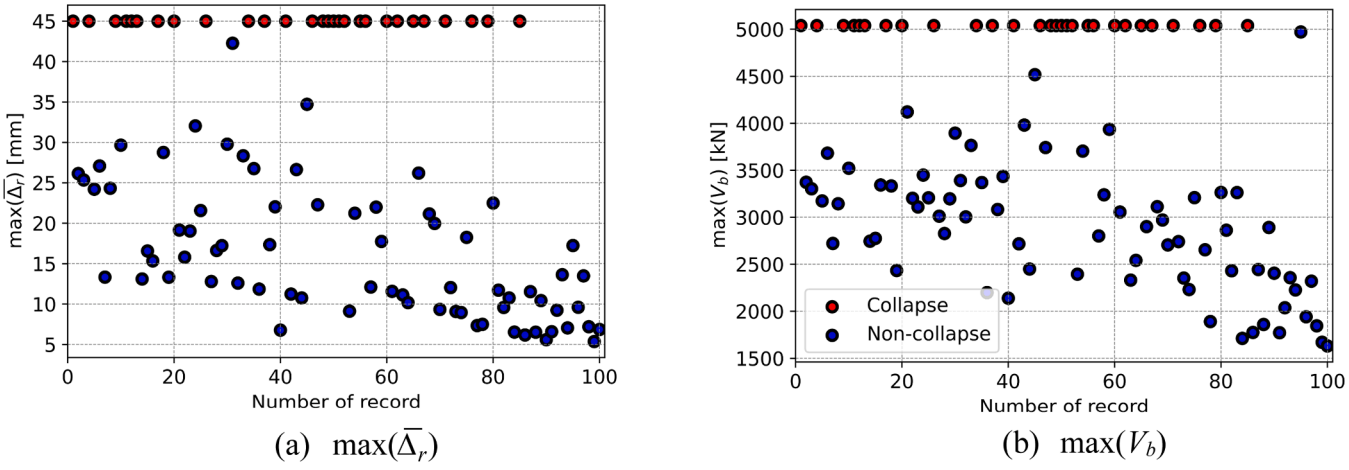

Fig. 10. Results of cloud analyses — Lausanne Malley building.

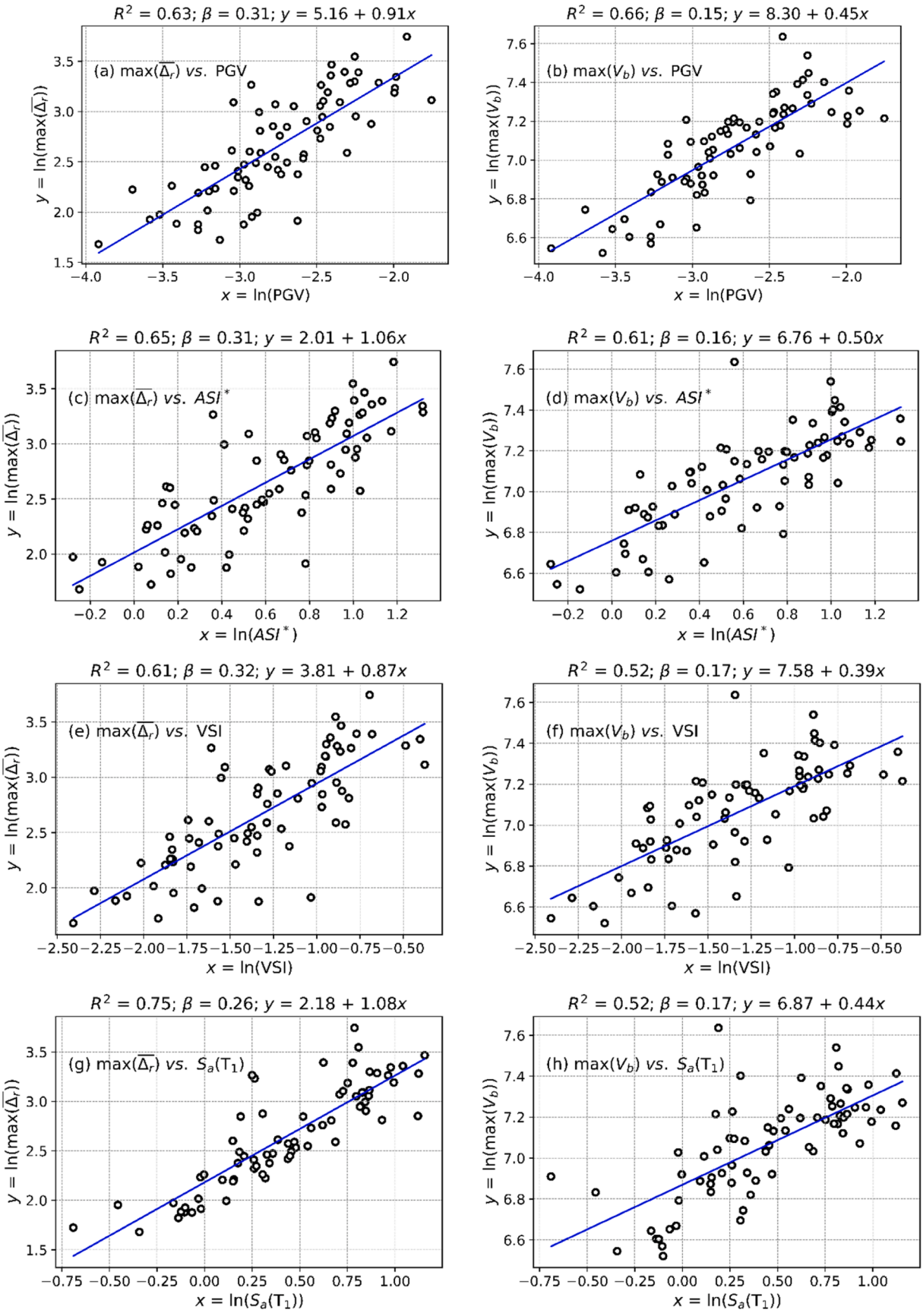

Fig. 11. PSDM for individual IMs — Lausanne Malley building.

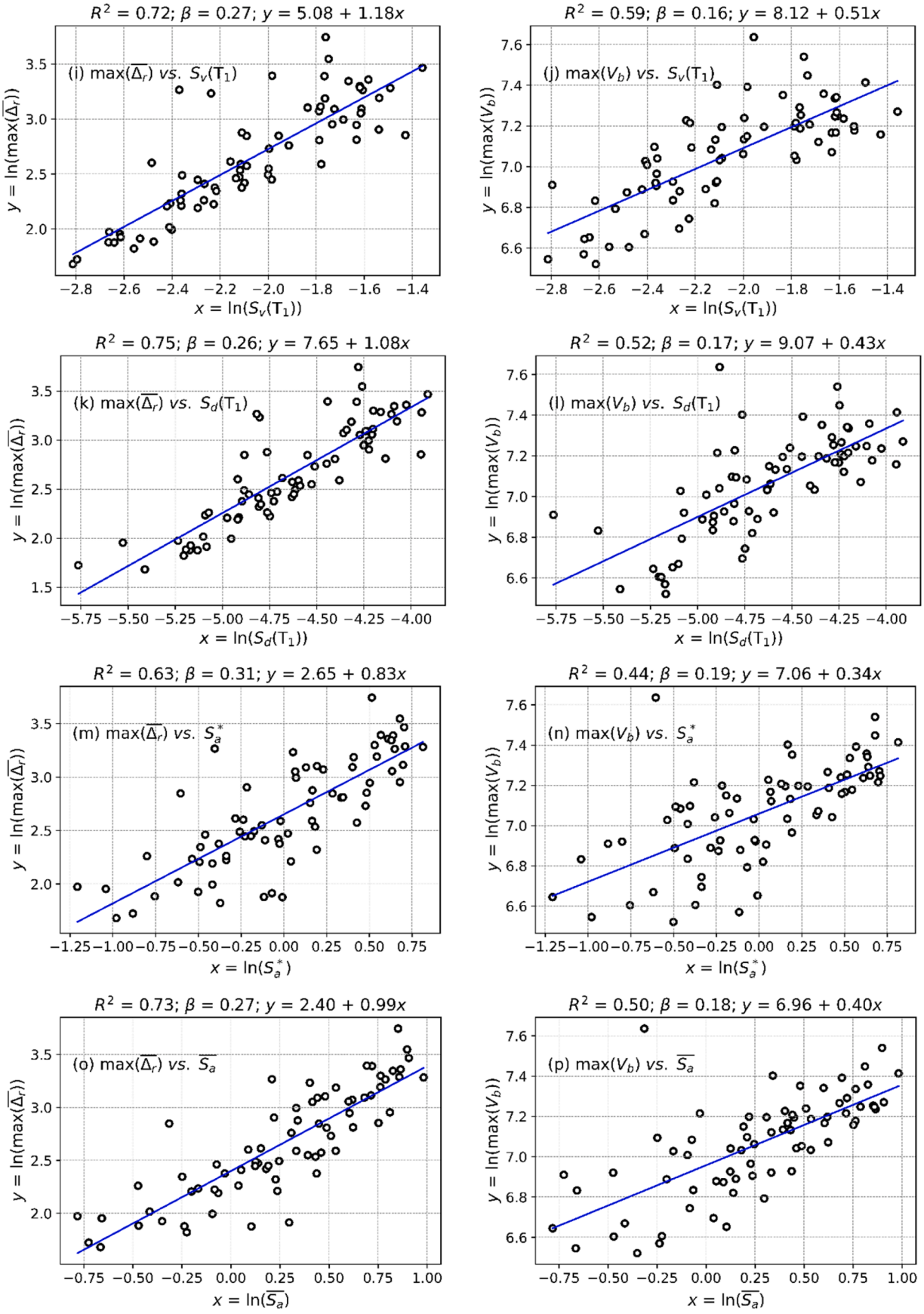

Fig. 11. (*continued*).

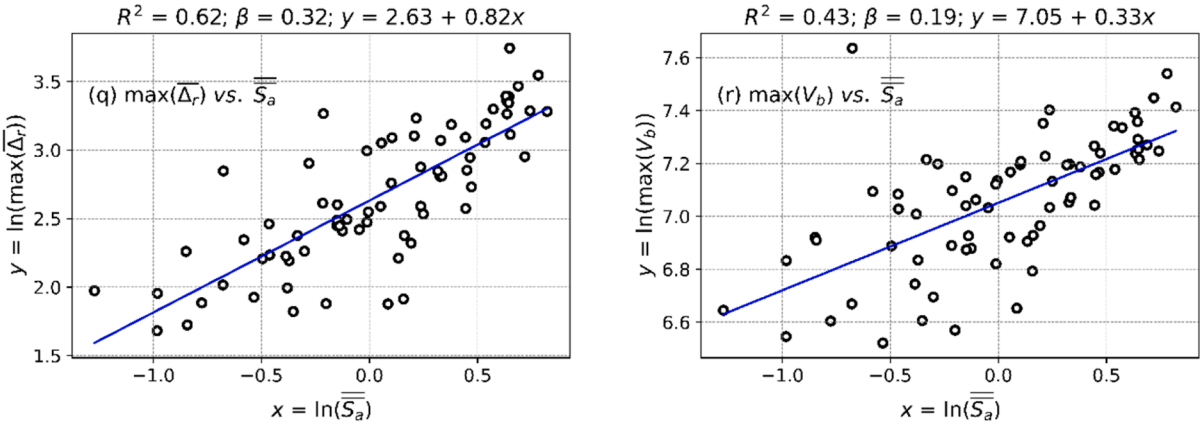

Fig. 11. (*continued*).

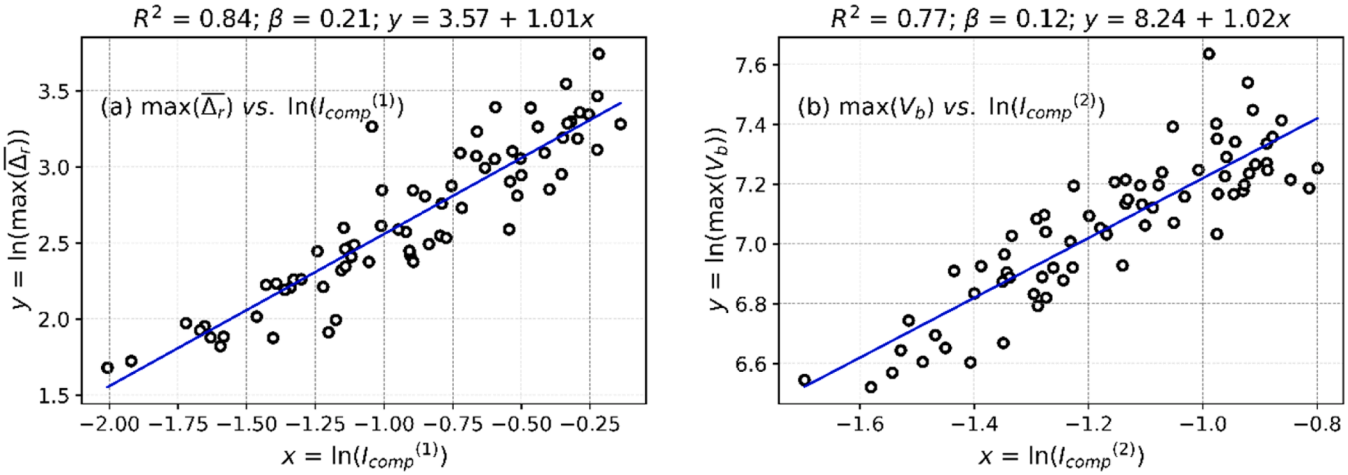

Fig. 12. PSDM with I_{comp} as independent variable using LASSO regression — Lausanne Malley building.

Table 4
Regression coefficients — Lausanne Malley building.

EDP	Regression coefficients θ_i									
	PGV	ASI*	VSI	ASI	$S_a(T_1)$	$S_v(T_1)$	$S_d(T_1)$	S_a*	$\overline{S_a}$	$\overline{\overline{S_a}}$
max($\overline{\Delta_r}$)	0.62	0.00	−0.35	0.62	0.00	0.00	−0.02	0.30	0.00	0.62
max(V_b)	0.45	0.23	−0.35	0.00	0.26	0.00	0.00	0.00	0.00	0.45

as well. The implementation of Eq. (4) requires the collapse DS to be bounded by a user-defined limit in order to account for very large data points that can be obtained from the collapse or instability of the numerical model. These limits answer to the asymptotic values of max($\overline{\Delta_r}$) defined previously in Sections 4.4.1 and 4.4.2 as 40 mm and 45 mm for the Holsteiner Hof and Lausanne Maley, respectively (See Figs. 6a and a). A similar approach for the derivation of fragility functions can be found in [46,52,53].

Table 5
Definition of the DSs for seismic assessment of each case study building [116, 125–127].

DS	Level of *edp*	
	Holsteiner Hof	*Lausanne Malley*
Global collapse	$edp \geq 40$ mm	$edp \geq 45$ mm
Collapse prevention	25 mm $\leq edp <$ 40 mm	25 mm $\leq edp <$ 45 mm
Moderate to severe	15 mm $\leq edp <$ 25 mm	15 mm $\leq edp <$ 25 mm
Slight to moderate	10 mm $\leq edp <$ 15 mm	10 mm $\leq edp <$ 15 mm

For the sake of simplicity, four DSs are identified after performing the non-linear dynamic analysis on each case study building. These DSs are defined as (*i*) Global collapse; (*ii*) Collapse prevention; (*iii*) Moderate to severe; and (*iv*) Slight to moderate damage, and they are linked to different *edp* levels in terms of the max($\overline{\Delta_r}$). The levels of *edp* were estimated from the equivalence of drift-based DSs for the same buildings [116] and validated through observations in historical masonry structures with similar features [125–127]. Table 5 provides the levels of *edp* associated with the four DS that are considered in the fragility assessment of each case study building. It should be stressed that such limits correspond to reference values from the literature since the objective of this paper is not the investigation of global limits of EDPs at different performance levels. Another relevant feature of the fragility curves derived in this study is that they consider a unique value of β (standard deviation) for all DS, as these curves are a direct result of the global regression models analysed previously. As in the previous section, the discussion of the fragility assessment is presented for each case study

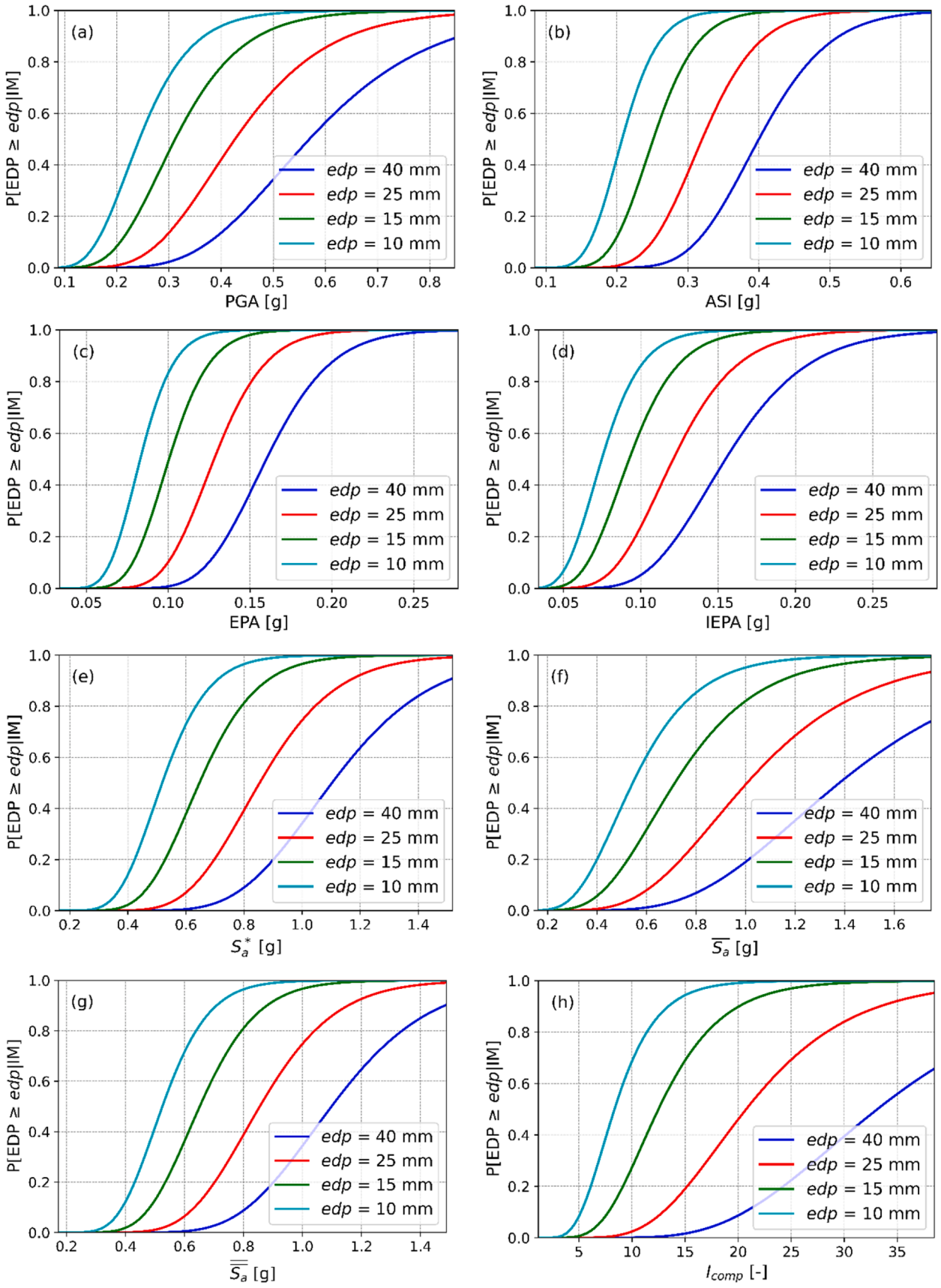

Fig. 13. Comparison of fragility curves based on IM parameter — Holsteiner Hof building.

building.

5.1. Holsteiner Hof

Fig. 13 shows the comparison of fragility curves derived for each of the preselected IMs with $R^2 \geq 0.6$ and the I_{comp}. Using these curves, the probability of exceedance of various levels of *edp* can be estimated from prior knowledge of a specific value of IM. For instance, the probability of collapse of the Holsteiner Hof building at PGA = 0.50 g is less than <40 %. Regardless of the improvements gained with I_{comp} within the PSDMs (e.g., higher R^2, less dispersion, and constant practicability), one major drawback is that units for this metric are not well defined since it is no longer a physical parameter but rather numerical, as previously discussed in Section 4.3. Thus, the comparison among curves with other IMs as independent variables cannot be direct. To overcome this limitation min-max normalization is applied to the values of IM, thus, they can be contrasted. Within this process, regardless of the unit, the maximum value of IM for each curve gets transformed into a 1, and every other value gets transformed into a decimal between 0 and 1. A similar approach for comparison of fragility in terms of different IMs was presented in [49,52]. Fig. 14 presents the fragility curves, reorganized at different levels of *edp*, considering the normalized values of IM in the x-axis through the min-max scaling.

It is seen that the S_a*, $\overline{S_a}$, $\overline{\overline{S_a}}$, and I_{comp} deliver less conservative predictions when compared to the other IMs. As mentioned previously, these metrics take into account the occurrence of damage during the analysis through the lengthening of structural periods. Moreover, these predictions are in agreement with the distribution of the empirical data within the regression models depicted in Fig. 7 and Fig. 8. Specifically, at *edp*s equal to 40 mm and 25 mm (i.e., collapse and near collapse DSs) the prediction of exceedance is less conservative using the I_{comp}, and its performance is comparable with the results of S_a*, $\overline{S_a}$, and $\overline{\overline{S_a}}$ as well as PGA. For less critical DSs, the performance of I_{comp} seems to be around the average of the predictions obtained using the other IMs. Thus, for such DSs (*edp* = 15 mm; *edp* = 10 mm) good estimations of the dynamic response can be achieved using any of the preselected IM parameters ($R^2 \geq 0.60$) as the independent variable.

5.2. Lausanne Malley

The fragility curves in terms of PGV, ASI*, VSI, $S_a(T_1)$, $S_v(T_1)$, $S_d(T_1)$, S_a*, $\overline{S_a}$, $\overline{\overline{S_a}}$, and I_{comp} are depicted in Fig. 15. Although comparison cannot be made directly with the fragility plots derived for the Holsteiner Hof building, it can be easily inferred that the Lausanne Malley building denotes a more vulnerable masonry structure. For instance, a probability of collapse higher than 80 % is computed for PGV = 0.3 m/s or $S_a(T_1)$ = 0.60 g. In general, the performance of all IMs under analysis, including I_{comp}, seems comparable regardless of the DS. To validate this statement, normalized fragility curves are presented in Fig. 16 separately as the probability of exceedance of each level of *edp* defined in Table 5. Effectively, the prediction of exceeding the corresponding value of *edp* at each DS is similar for any of the assessed IMs, being the prediction computed through I_{comp} approximately on the average of all predictions. This behaviour can be related to the number of preselected IMs (larger than for the Holsteiner Hof building) with acceptable levels of correlation and comparable performance, as it was previously depicted in Fig. 11. Moreover, Fig. 16(c) and (d) highlight the large probability of exceeding *edp* levels of 15 mm and 10 mm (i.e., severe to moderate damage) at relatively lower levels of IM. Lastly, the observation of probabilities higher than 0 at IM levels equal or near to 0 can be

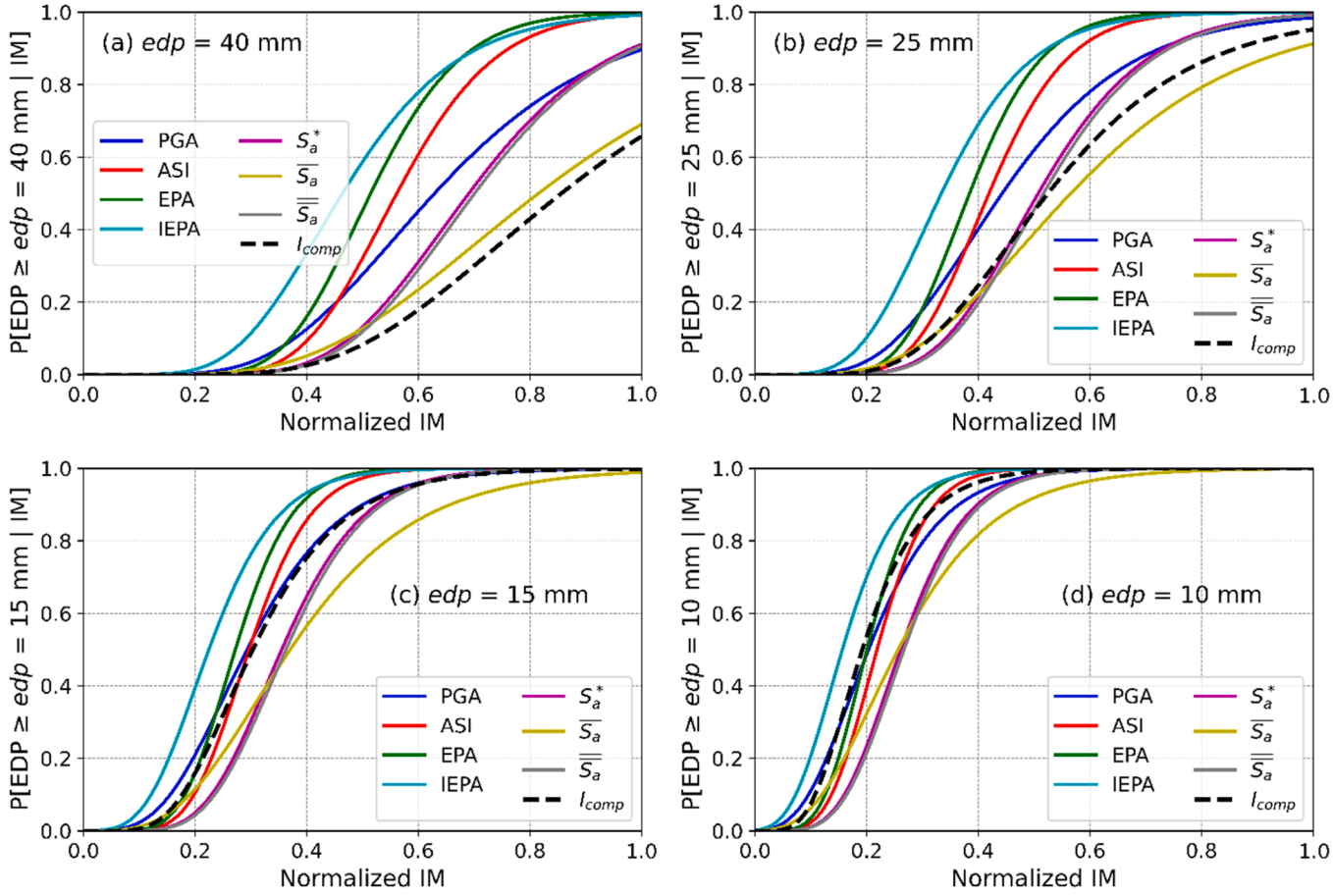

Fig. 14. Normalized fragility curves at different levels of edp — Holsteiner Hof building.

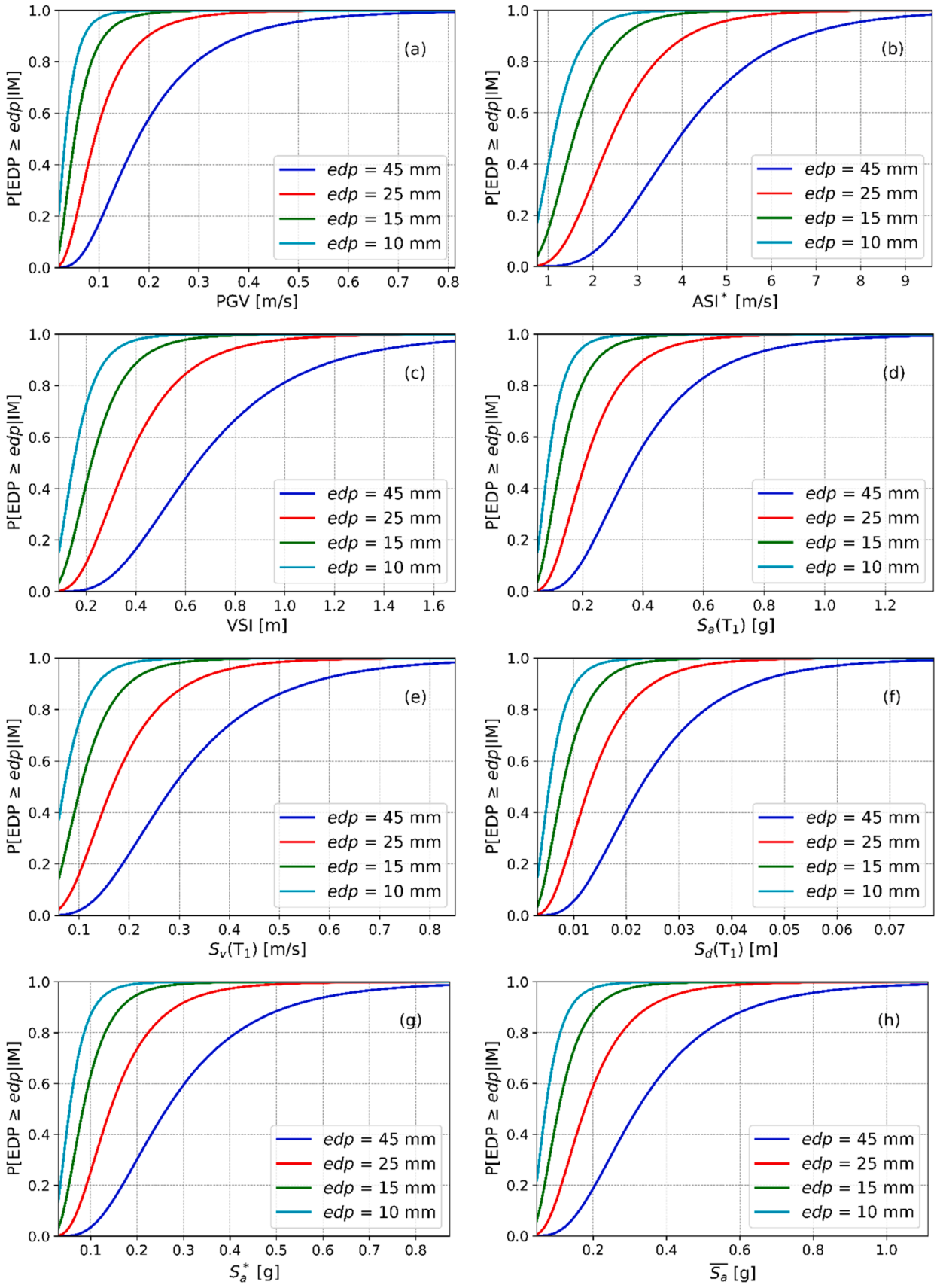

Fig. 15. Comparison of fragility curves based on IM parameter — Lausanne Malley building.

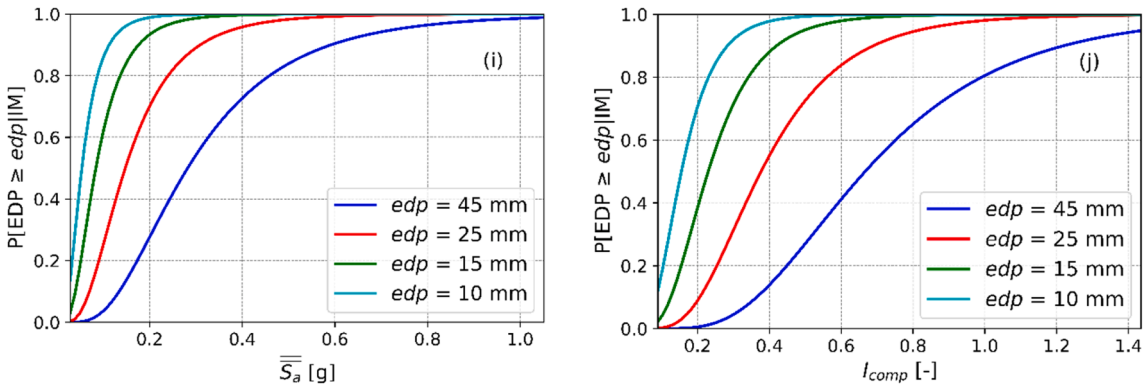

Fig. 15. (*continued*).

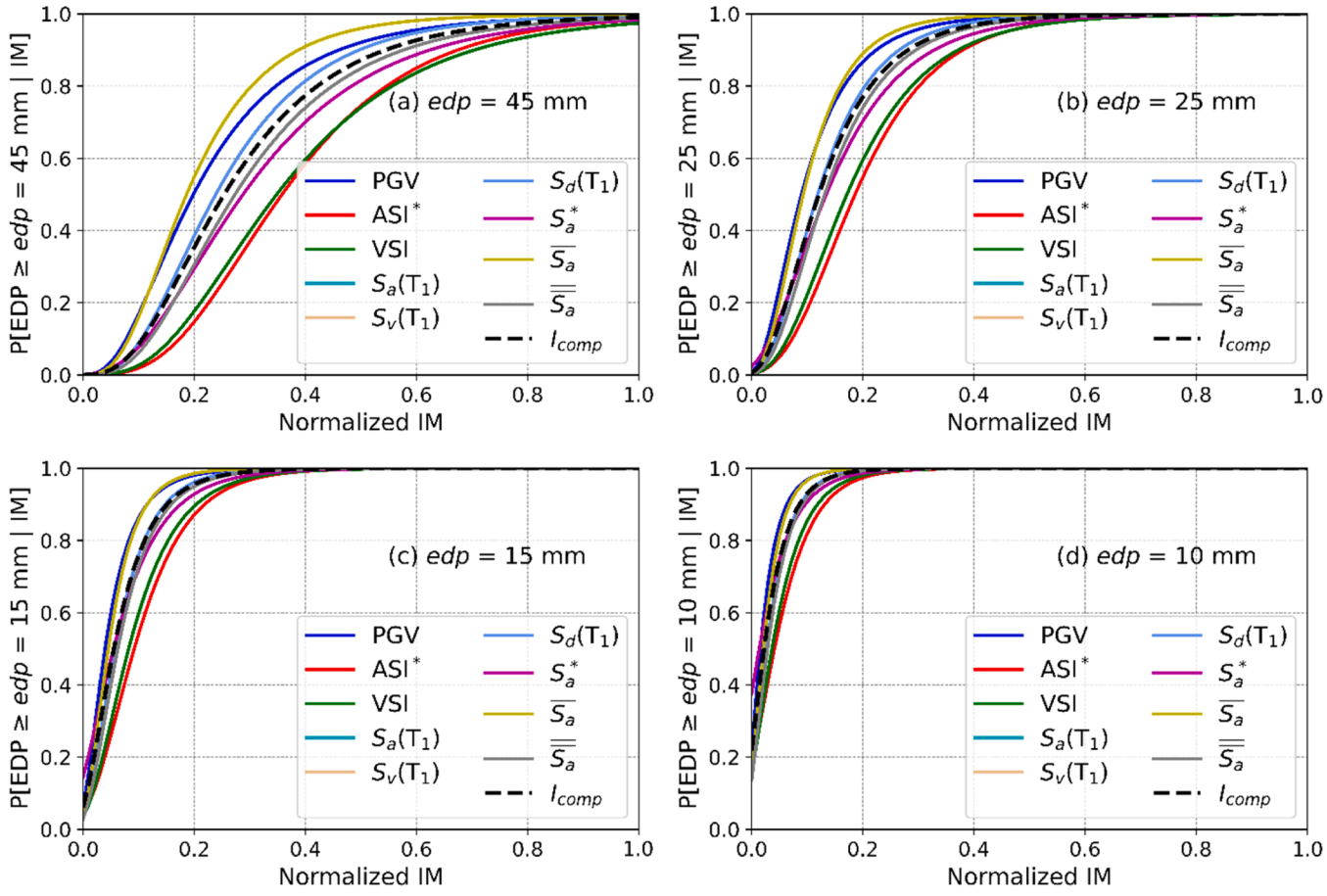

Fig. 16. Normalized fragility curves at different levels of edp — Lausanne Malley building.

attributed to the limitations of PSDM-based fragility using single β values. Within such global regression models low-intensity records that can induce slight to moderate damage are limited, making it difficult the characterisation of DSs defined by lower levels of *epd*. Similar observations were briefly reported by Hariri-Ardebili and Saouma [46] in fragility surfaces of concrete dams at low levels of *edp*. In this regard, some other methodologies can be used, such as IDA in [116], for the characterisation of dynamic behaviour at different performance levels, or other cloud-based methods to obtain mean and standard deviation independently for each DS [128,129].

6. Conclusions

Identification of optimal intensity measures (IMs) and probabilistic seismic demand (PSDA) of two case study historical masonry buildings was addressed in this paper. Both buildings were modelled in the OpenSees software package using three-dimensional macroelements that consider the in-plane (IP) and out-of-plane (OOP) response of masonry walls. A large set of accelerograms ($n = 100$) was selected using unconditional selection (i.e., non-dependent from structural periods). A total of 84 metrics, including seismological parameters, and IMs subdivided into period and duration-related, ground motion dependent scalars, ground motion dependent compound, structure-independent spectral, and structure-dependent spectral IMs were examined

according to the notions of efficiency, practicability, proficiency, and sufficiency. A composed measure, calibrated for each engineering demand parameter (EDP) and structure, was further proposed as a linear combination in logarithmic space of the IMs with the best correlation in the EDP vs. IM regression. Consistent probabilistic seismic demand models (PSDMs) and fragility curves were derived from cloud analysis afterwards.

For the Holsteiner Hof building the best ranked IMs corresponded to PGA, EPA, IEPA, ASI, S_a*, $\overline{S_a}$ and $\overline{\overline{S_a}}$; all of them acceleration-related metrics. Great performance was observed in the PSDMs, even at collapse damage state (DS) (independently of IP or OOP mechanism), when structural damage and period lengthening was accounted for using S_a*, $\overline{S_a}$, and $\overline{\overline{S_a}}$. On the other hand, 9 IMs were identified as the most suitable for the prediction of the seismic performance of the Lausanne Malley building. These 9 measures were a combination of acceleration, velocity and even displacement-related IMs, including PGV, ASI*, VSI, $S_a(T_1)$, $S_v(T_1)$, $S_d(T_1)$, S_a*, $\overline{S_a}$, and $\overline{\overline{S_a}}$. The influence of velocity and displacement metrics, besides acceleration-related ones, is consistent with former findings on the OOP seismic resistance of masonry walls. For both case study buildings, the derived I_{comp} showed clear enhancements in terms of correlation, efficiency, practicability, and proficiency, increasing the values of correlation up to 0.84 and 0.81 for the max($\overline{\Delta_r}$) and max(V_b), compared to a maximum of R^2 equals to 0.75 and 0.80 for the same EDPs that was obtained through PSDMs with individual IMs. Regarding the fragility analysis of the Holsteiner Hof building, S_a*, $\overline{S_a}$, $\overline{\overline{S_a}}$, and I_{comp} provided less conservative predictions at the collapse DS ($edp = 40$ mm). Similar behaviour was observed at near collapse, while for severe and moderate DS the predictions were comparable regardless of the IM parameter. Conversely, the Lausanne Malley building was found to be significantly more vulnerable with similar predictions in the fragility analysis at different DSs regardless of the IM input parameter.

Finally, the proposed framework seems adequate for the identification of adequate IMs and derivation of optimal composed measures for the PSDA of historic masonry buildings. Certainly, the derivation of an optimal composite IM is useful to enhance the EDP-IM correlation with a reasonable computational burden. This metric denotes a numerical parameter specific to each building and EDP with no associated units. Moreover, the methodology based on Lasso regression demonstrated the capability for identification of the most relevant IMs, especially for the case of complex structural systems with a large influence of non-linear effects where the dynamic behaviour is difficult to predict employing single or conventional metrics. Since the numerical results derived from this research are structure-specific (i.e., dependent on the case study under analysis) future work should focus on different structural typologies and analysing the consistency of the fragility curves derived from the cloud-based approach against other methodologies such as multiple-record incremental dynamic analyses.

CRediT authorship contribution statement

Daniel Caicedo: Writing – original draft, Visualization, Validation, Software, Methodology, Investigation, Formal analysis, Conceptualization. **Igor Tomić:** Writing – review & editing, Visualization, Validation, Supervision, Software, Methodology, Investigation, Conceptualization. **Shaghayegh Karimzadeh:** Writing – review & editing, Visualization, Supervision, Methodology, Investigation, Conceptualization. **Vasco Bernardo:** Writing – review & editing, Visualization, Supervision, Methodology, Investigation, Conceptualization. **Katrin Beyer:** Writing – review & editing, Visualization, Supervision, Methodology, Conceptualization. **Paulo B. Lourenço:** Writing – review & editing, Supervision, Project administration, Methodology, Funding acquisition, Conceptualization.

Declaration of competing interest

The authors declare that they have no known competing financial interests or personal relationships that could have appeared to influence the work reported in this paper.

Acknowledgments

This study has been partly funded by the STAND4HERITAGE project that has received funding from the European Research Council (ERC) under the European Union's Horizon 2020 research and innovation program (Grant agreement No 833123), as an Advanced Grant. This work was also partly financed by FCT / MCTES through national funds (PIDDAC) under the R&D Unit Institute for Sustainability and Innovation in Structural Engineering (ISISE), under reference UIDB / 04029/2020 (doi.org/10.54499/UIDB/04029/2020), and under the Associate Laboratory Advanced Production and Intelligent Systems ARISE under reference LA/P/0112/2020. This work is partly financed by national funds through FCT - Foundation for Science and Technology, under grant agreement 2023.01101.BD attributed to the first author. The second author was supported by the Swiss National Science Foundation through grant 200021_175903/1 Equivalent frame models for the in-plane and out-of-plane response of unreinforced masonry buildings.

Appendix

Table A1, Table A2

Table A1
Values for the assessment of the optimal IM — Holsteiner Hof building.

EDP	max($\overline{\Delta_r}$)									max(V_b)								
IM	b	$\beta_{EDP\|IM}$	ζ	R^2	*p-value*					b	$\beta_{EDP\|IM}$	ζ	R^2	*p-value*				
					M_w	R_{epi}	R_{rup}	R_{JB}	R_{hyp}					M_w	R_{epi}	R_{rup}	R_{JB}	R_{hyp}
Seismological IMs																		
M_w	0.74	0.77	1.04	0.01	0.96	0.02	0.01	0.01	0.02	0.25	0.24	0.96	0.02	0.98	0.00	0.00	0.00	0.00
V_{s30}	0.14	0.77	5.52	0.01	0.32	0.11	0.06	0.06	0.11	0.04	0.24	5.50	0.01	0.29	0.04	0.02	0.02	0.04
R_{epi}	−0.20	0.75	−3.78	0.05	0.01	0.79	0.95	0.98	0.80	−0.07	0.24	−3.20	0.07	0.00	0.94	0.82	0.83	0.94
R_{rup}	−0.24	0.75	−3.08	0.06	0.00	0.62	0.85	0.83	0.62	−0.08	0.24	−2.83	0.07	0.00	0.88	0.90	0.90	0.87
R_{JB}	−0.20	0.75	−3.65	0.06	0.01	0.70	0.95	0.92	0.71	−0.07	0.24	−3.15	0.07	0.00	0.87	0.90	0.91	0.87
R_{hyp}	−0.22	0.75	−3.39	0.05	0.01	0.78	0.97	0.99	0.78	−0.08	0.24	−2.98	0.06	0.00	0.98	0.78	0.78	0.97
Period and duration-related IMs																		
$D_{5–75}$	−0.35	0.72	−2.08	0.12	0.00	0.91	0.85	0.89	0.93	−0.11	0.23	−2.14	0.11	0.00	0.65	0.46	0.47	0.64

(*continued on next page*)

Table A1 (*continued*)

EDP	$\max(\overline{\Delta_r})$									$\max(V_b)$								
IM	*b*	$\beta_{EDP\|IM}$	ζ	R^2	*p-value*					*b*	$\beta_{EDP\|IM}$	ζ	R^2	*p-value*				
					M_w	R_{epi}	R_{rup}	R_{JB}	R_{hyp}					M_w	R_{epi}	R_{rup}	R_{JB}	R_{hyp}
$D_{5–95}$	−0.39	0.73	−1.85	0.11	0.00	0.92	0.83	0.87	0.94	−0.12	0.23	−1.94	0.10	0.00	0.62	0.43	0.44	0.62
Tp	−0.10	0.77	−7.71	0.01	0.22	0.15	0.08	0.08	0.15	−0.03	0.24	−7.55	0.01	0.19	0.05	0.03	0.03	0.05
Tm	−0.11	0.77	−7.24	0.00	0.18	0.18	0.09	0.10	0.17	−0.07	0.24	−3.62	0.01	0.10	0.10	0.05	0.05	0.10
Ground motion dependent scalars IMs																		
PGA	1.46	0.50	0.35	**0.57**	0.01	0.07	0.11	0.09	0.08	0.49	0.15	0.30	**0.63**	0.00	0.17	0.24	0.21	0.18
PGV	0.97	0.62	0.64	0.36	0.01	0.00	0.00	0.00	0.00	0.30	0.20	0.65	0.35	0.02	0.00	0.00	0.00	0.00
PGD	0.23	0.74	3.23	0.08	0.31	0.00	0.00	0.00	0.00	0.08	0.23	3.03	0.10	0.28	0.00	0.00	0.00	0.00
a_{RMS}	1.12	0.59	0.53	0.41	0.31	0.08	0.05	0.05	0.09	0.34	0.19	0.57	0.37	0.44	0.02	0.01	0.01	0.02
v_{RMS}	0.45	0.70	1.57	0.16	0.09	0.00	0.00	0.00	0.00	0.13	0.23	1.77	0.13	0.20	0.00	0.00	0.00	0.00
u_{RMS}	0.15	0.75	4.85	0.06	0.47	0.00	0.00	0.00	0.00	0.05	0.24	4.63	0.06	0.46	0.00	0.00	0.00	0.00
I_A	0.83	0.59	0.71	0.42	0.05	0.00	0.00	0.00	0.00	0.28	0.17	0.62	0.49	0.02	0.00	0.00	0.00	0.00
CAV	0.27	0.76	2.82	0.03	0.81	0.02	0.01	0.01	0.02	0.12	0.24	2.04	0.05	0.99	0.00	0.00	0.00	0.00
CAD	0.07	0.77	10.28	0.01	0.56	0.04	0.02	0.02	0.04	0.03	0.24	7.12	0.02	0.67	0.01	0.00	0.00	0.01
SED	0.16	0.74	4.54	0.08	0.43	0.00	0.00	0.00	0.00	0.05	0.23	4.48	0.08	0.46	0.00	0.00	0.00	0.00
Ground motion dependent compound IMs																		
PGV/PGA	−0.06	0.77	−13.43	0.00	0.18	0.17	0.09	0.10	0.17	−0.04	0.24	−5.93	0.01	0.09	0.11	0.06	0.06	0.11
PGV^2/PGA	0.29	0.73	2.54	0.10	0.39	0.00	0.00	0.00	0.00	0.08	0.23	2.82	0.08	0.55	0.00	0.00	0.00	0.00
I_a	1.61	0.56	0.35	0.48	0.72	0.22	0.15	0.17	0.22	0.55	0.16	0.30	0.55	0.66	0.05	0.03	0.03	0.05
I_v	0.51	0.74	1.44	0.08	0.52	0.00	0.00	0.00	0.00	0.16	0.24	1.46	0.08	0.58	0.00	0.00	0.00	0.00
I_d	0.13	0.76	5.69	0.04	0.79	0.01	0.00	0.00	0.01	0.05	0.24	5.20	0.04	0.74	0.00	0.00	0.00	0.00
I_F	0.63	0.69	1.10	0.19	0.10	0.00	0.00	0.00	0.00	0.20	0.22	1.12	0.18	0.13	0.00	0.00	0.00	0.00
I_Z	−0.79	0.69	−0.87	0.20	0.10	0.28	0.19	0.21	0.27	−0.22	0.22	−1.00	0.16	0.10	0.09	0.06	0.06	0.09
I_C	0.53	0.68	1.29	0.22	0.16	0.00	0.00	0.00	0.00	0.16	0.22	1.39	0.19	0.25	0.00	0.00	0.00	0.00
SIR	0.64	0.52	0.80	0.55	0.00	0.07	0.12	0.10	0.08	0.21	0.15	0.71	0.61	0.00	0.18	0.26	0.24	0.20
Structure-independent spectral IMs																		
EPA	2.00	0.40	0.20	**0.73**	0.24	0.34	0.40	0.38	0.34	0.66	0.11	0.17	**0.80**	0.14	0.84	0.87	0.89	0.81
EPV	0.77	0.67	0.88	0.24	0.45	0.00	0.00	0.00	0.00	0.23	0.22	0.94	0.22	0.58	0.00	0.00	0.00	0.00
IEPA	1.75	0.49	0.28	**0.60**	0.21	0.69	0.83	0.81	0.69	0.62	0.12	0.20	**0.74**	0.10	0.95	0.85	0.83	0.98
IEPV	0.88	0.64	0.73	0.31	0.14	0.00	0.00	0.00	0.00	0.24	0.21	0.88	0.23	0.33	0.00	0.00	0.00	0.00
HI	0.61	0.69	1.14	0.19	0.25	0.00	0.00	0.00	0.00	0.19	0.22	1.17	0.18	0.30	0.00	0.00	0.00	0.00
ASI	2.00	0.40	0.20	**0.73**	0.24	0.34	0.40	0.38	0.34	0.66	0.11	0.17	**0.80**	0.14	0.84	0.87	0.89	0.81
ASI*	1.40	0.56	0.40	0.46	0.07	0.00	0.00	0.00	0.00	0.44	0.18	0.41	0.46	0.09	0.00	0.00	0.00	0.00
VSI	0.96	0.64	0.67	0.31	0.11	0.00	0.00	0.00	0.00	0.30	0.20	0.67	0.31	0.13	0.00	0.00	0.00	0.00
DSI	0.16	0.75	4.71	0.04	0.86	0.01	0.01	0.01	0.01	0.06	0.24	3.97	0.05	0.74	0.00	0.00	0.00	0.00
Structure-dependent spectral IMs																		
$S_a(T_1)$	0.95	0.60	0.63	0.39	0.02	0.25	0.36	0.32	0.26	0.33	0.18	0.55	0.46	0.01	0.41	0.53	0.51	0.42
$S_a(T_2)$	0.95	0.60	0.63	0.39	0.02	0.25	0.36	0.32	0.26	0.33	0.18	0.55	0.46	0.01	0.41	0.53	0.51	0.42
$S_a(T_3)$	0.77	0.63	0.82	0.34	0.00	0.13	0.21	0.18	0.14	0.27	0.19	0.68	0.43	0.00	0.15	0.22	0.20	0.15
$S_a(T_4)$	0.77	0.63	0.82	0.34	0.00	0.13	0.21	0.18	0.14	0.27	0.19	0.68	0.43	0.00	0.15	0.22	0.20	0.15
$S_a(T_5)$	0.77	0.63	0.82	0.34	0.00	0.13	0.21	0.18	0.14	0.27	0.19	0.68	0.43	0.00	0.15	0.22	0.20	0.15
$S_a(T_6)$	0.77	0.63	0.82	0.34	0.00	0.13	0.21	0.18	0.14	0.27	0.19	0.68	0.43	0.00	0.15	0.22	0.20	0.15
$S_a(T_7)$	0.77	0.63	0.82	0.34	0.00	0.13	0.21	0.18	0.14	0.27	0.19	0.68	0.43	0.00	0.15	0.22	0.20	0.15
$S_a(T_8)$	0.77	0.63	0.82	0.34	0.00	0.13	0.21	0.18	0.14	0.27	0.19	0.68	0.43	0.00	0.15	0.22	0.20	0.15
$S_a(T_9)$	0.77	0.63	0.82	0.34	0.00	0.13	0.21	0.18	0.14	0.27	0.19	0.68	0.43	0.00	0.15	0.22	0.20	0.15
$S_a(T_{10})$	0.77	0.63	0.82	0.34	0.00	0.13	0.21	0.18	0.14	0.27	0.19	0.68	0.43	0.00	0.15	0.22	0.20	0.15
$S_v(T_1)$	0.71	0.64	0.90	0.31	0.02	0.33	0.47	0.42	0.35	0.24	0.20	0.80	0.36	0.01	0.54	0.69	0.66	0.55
$S_v(T_2)$	0.71	0.64	0.90	0.31	0.02	0.33	0.47	0.42	0.35	0.24	0.20	0.80	0.36	0.01	0.54	0.69	0.66	0.55
$S_v(T_3)$	0.51	0.67	1.32	0.25	0.01	0.28	0.41	0.38	0.30	0.18	0.20	1.13	0.31	0.00	0.37	0.50	0.48	0.39
$S_v(T_4)$	0.51	0.67	1.32	0.25	0.01	0.28	0.41	0.38	0.30	0.18	0.20	1.13	0.31	0.00	0.37	0.50	0.48	0.39
$S_v(T_5)$	0.51	0.67	1.32	0.25	0.01	0.28	0.41	0.38	0.30	0.18	0.20	1.13	0.31	0.00	0.37	0.50	0.48	0.39
$S_v(T_6)$	0.51	0.67	1.32	0.25	0.01	0.28	0.41	0.38	0.30	0.18	0.20	1.13	0.31	0.00	0.37	0.50	0.48	0.39
$S_v(T_7)$	0.51	0.67	1.32	0.25	0.01	0.28	0.41	0.38	0.30	0.18	0.20	1.13	0.31	0.00	0.37	0.50	0.48	0.39
$S_v(T_8)$	0.51	0.67	1.32	0.25	0.01	0.28	0.41	0.38	0.30	0.18	0.20	1.13	0.31	0.00	0.37	0.50	0.48	0.39
$S_v(T_9)$	0.51	0.67	1.32	0.25	0.01	0.28	0.41	0.38	0.30	0.18	0.20	1.13	0.31	0.00	0.37	0.50	0.48	0.39
$S_v(T_{10})$	0.51	0.67	1.32	0.25	0.01	0.28	0.41	0.38	0.30	0.18	0.20	1.13	0.31	0.00	0.37	0.50	0.48	0.39
$S_d(T_1)$	0.95	0.60	0.63	0.39	0.02	0.25	0.36	0.32	0.26	0.33	0.18	0.55	0.46	0.01	0.41	0.53	0.50	0.42
$S_d(T_2)$	0.95	0.60	0.63	0.39	0.02	0.25	0.36	0.32	0.26	0.33	0.18	0.55	0.46	0.01	0.41	0.53	0.50	0.42
$S_d(T_3)$	0.77	0.63	0.82	0.34	0.00	0.13	0.21	0.18	0.14	0.27	0.18	0.67	0.43	0.00	0.15	0.22	0.20	0.15
$S_d(T_4)$	0.77	0.63	0.82	0.34	0.00	0.13	0.21	0.18	0.14	0.27	0.18	0.67	0.43	0.00	0.15	0.22	0.20	0.15
$S_d(T_5)$	0.77	0.63	0.82	0.34	0.00	0.13	0.21	0.18	0.14	0.27	0.18	0.67	0.43	0.00	0.15	0.22	0.20	0.15
$S_d(T_6)$	0.77	0.63	0.82	0.34	0.00	0.13	0.21	0.18	0.14	0.27	0.18	0.67	0.43	0.00	0.15	0.22	0.20	0.15
$S_d(T_7)$	0.77	0.63	0.82	0.34	0.00	0.13	0.21	0.18	0.14	0.27	0.18	0.67	0.43	0.00	0.15	0.22	0.20	0.15
$S_d(T_8)$	0.77	0.63	0.82	0.34	0.00	0.13	0.21	0.18	0.14	0.27	0.18	0.67	0.43	0.00	0.15	0.22	0.20	0.15
$S_d(T_9)$	0.77	0.63	0.82	0.34	0.00	0.13	0.21	0.18	0.14	0.27	0.18	0.67	0.43	0.00	0.15	0.22	0.20	0.15
$S_d(T_{10})$	0.77	0.63	0.82	0.34	0.00	0.13	0.21	0.18	0.14	0.27	0.18	0.67	0.43	0.00	0.15	0.22	0.20	0.15
$S_a(T = 0.1\ s)$	0.77	0.63	0.82	0.34	0.00	0.13	0.21	0.18	0.14	0.27	0.19	0.68	0.43	0.00	0.15	0.22	0.20	0.15
$S_a(T = 0.2\ s)$	1.18	0.57	0.48	0.46	0.11	0.72	0.93	0.88	0.75	0.42	0.16	0.38	0.58	0.05	0.99	0.81	0.83	0.98
$S_a(T = 0.5\ s)$	1.19	0.61	0.52	0.37	0.63	0.01	0.00	0.00	0.01	0.31	0.21	0.69	0.24	0.97	0.00	0.00	0.00	0.00
$S_a(T = 1.0\ s)$	0.45	0.72	1.58	0.14	0.73	0.01	0.00	0.00	0.01	0.13	0.23	1.77	0.11	0.90	0.00	0.00	0.00	0.00
$\boldsymbol{S_a}^*$	1.72	0.43	0.25	**0.68**	0.11	0.13	0.16	0.15	0.13	0.55	0.14	0.25	**0.69**	0.08	0.51	0.53	0.54	0.49
$\overline{S_a}$	1.34	0.52	0.39	**0.54**	0.04	0.24	0.33	0.30	0.25	0.48	0.14	0.29	**0.68**	0.01	0.28	0.37	0.34	0.29
$\overline{\overline{S_a}}$	1.75	0.43	0.25	**0.69**	0.17	0.27	0.32	0.30	0.27	0.59	0.11	0.19	**0.78**	0.09	0.59	0.61	0.62	0.58

(*continued on next page*)

Table A1 (*continued*)

EDP	$\max(\overline{\Delta_r})$									$\max(V_b)$								
IM	*b*	$\beta_{EDP\|IM}$	ζ	R^2	*p-value*					*b*	$\beta_{EDP\|IM}$	ζ	R^2	*p-value*				
					M_w	R_{epi}	R_{rup}	R_{JB}	R_{hyp}					M_w	R_{epi}	R_{rup}	R_{JB}	R_{hyp}
$S_a^{1\text{-}to\text{-}2}$	0.95	0.60	0.63	0.39	0.02	0.25	0.36	0.32	0.26	0.33	0.18	0.55	0.46	0.01	0.41	0.53	0.51	0.42
$S_a^{1\text{-}to\text{-}3}$	0.95	0.60	0.63	0.39	0.02	0.24	0.36	0.32	0.26	0.33	0.18	0.55	0.46	0.01	0.41	0.53	0.50	0.41
$S_a^{1\text{-}to\text{-}4}$	0.95	0.60	0.63	0.39	0.02	0.21	0.31	0.28	0.22	0.33	0.18	0.55	0.46	0.01	0.35	0.46	0.43	0.35
$S_a^{1\text{-}to\text{-}5}$	0.95	0.60	0.63	0.39	0.02	0.21	0.31	0.28	0.22	0.33	0.18	0.55	0.46	0.01	0.35	0.46	0.43	0.35
$S_a^{1\text{-}to\text{-}6}$	0.94	0.60	0.64	0.39	0.01	0.17	0.26	0.23	0.18	0.33	0.18	0.55	0.47	0.00	0.27	0.36	0.34	0.27
$S_a^{1\text{-}to\text{-}7}$	0.94	0.60	0.64	0.39	0.01	0.17	0.26	0.23	0.18	0.33	0.18	0.55	0.47	0.00	0.27	0.36	0.34	0.27
$S_a^{1\text{-}to\text{-}8}$	0.94	0.60	0.64	0.39	0.01	0.17	0.26	0.23	0.18	0.33	0.18	0.55	0.47	0.00	0.27	0.36	0.34	0.27
$S_a^{1\text{-}to\text{-}9}$	0.94	0.60	0.64	0.39	0.01	0.17	0.26	0.23	0.18	0.33	0.18	0.55	0.47	0.00	0.27	0.36	0.34	0.27
$S_a^{1\text{-}to\text{-}10}$	0.94	0.60	0.64	0.39	0.01	0.17	0.26	0.23	0.18	0.33	0.18	0.55	0.47	0.00	0.27	0.36	0.34	0.27

Table A2
Values for the assessment of the optimal IM — Lausanne Malley building.

EDP	$\max(\overline{\Delta_r})$									$\max(V_b)$								
IM	*b*	$\beta_{EDP\|IM}$	ζ	R^2	*p-value*					*b*	$\beta_{EDP\|IM}$	ζ	R^2	*p-value*				
					M_w	R_{epi}	R_{rup}	R_{JB}	R_{hyp}					M_w	R_{epi}	R_{rup}	R_{JB}	R_{hyp}
Seismological IMs																		
M_w	1.36	0.49	0.36	0.09	0.95	0.23	0.15	0.17	0.21	0.27	0.25	0.91	0.02	0.95	0.06	0.03	0.03	0.06
V_{s30}	−0.15	0.51	−3.43	0.02	0.01	0.69	0.99	0.93	0.75	−0.06	0.25	−4.43	0.01	0.22	0.21	0.12	0.12	0.20
R_{epi}	0.00	0.52	334.01	0.00	0.01	0.69	0.96	0.90	0.75	−0.07	0.24	−3.29	0.07	0.01	0.47	0.69	0.66	0.50
R_{rup}	−0.02	0.52	−24.04	0.00	0.01	0.50	0.75	0.69	0.56	−0.08	0.24	−2.88	0.07	0.01	0.44	0.64	0.62	0.46
R_{JB}	−0.01	0.52	−47.62	0.00	0.01	0.57	0.83	0.77	0.63	−0.08	0.24	−3.13	0.08	0.01	0.38	0.57	0.54	0.40
R_{hyp}	−0.01	0.52	−97.42	0.00	0.01	0.63	0.90	0.84	0.69	−0.08	0.24	−3.05	0.06	0.01	0.53	0.75	0.73	0.55
Period and duration-related IMs																		
$D_{5\text{–}75}$	0.05	0.51	11.33	0.00	0.02	0.84	0.88	0.94	0.90	−0.08	0.24	−3.25	0.05	0.07	0.63	0.44	0.46	0.60
$D_{5\text{–}95}$	0.03	0.52	14.80	0.00	0.01	0.79	0.93	0.99	0.85	−0.10	0.24	−2.56	0.06	0.06	0.73	0.52	0.55	0.70
Tp	0.30	0.49	1.65	0.09	0.07	0.61	0.39	0.42	0.57	0.05	0.25	4.69	0.01	0.42	0.12	0.06	0.06	0.11
Tm	0.53	0.47	0.88	0.18	0.28	0.16	0.08	0.08	0.15	0.10	0.25	2.45	0.03	0.63	0.05	0.03	0.03	0.05
Ground motion dependent scalars IMs																		
PGA	0.52	0.47	0.91	0.17	0.00	0.02	0.05	0.04	0.03	0.40	0.19	0.47	0.43	0.03	0.07	0.10	0.08	0.08
PGV	0.91	0.31	0.34	**0.63**	0.64	0.63	0.60	0.66	0.59	0.45	0.15	0.33	**0.66**	0.00	0.00	0.00	0.00	0.00
PGD	0.38	0.40	1.07	0.39	0.25	0.07	0.06	0.06	0.06	0.14	0.22	1.51	0.24	0.06	0.00	0.00	0.00	0.00
a_{RMS}	0.51	0.45	0.88	0.24	0.17	0.39	0.54	0.50	0.43	0.30	0.20	0.66	0.36	0.49	0.30	0.24	0.23	0.31
v_{RMS}	0.48	0.40	0.82	0.41	0.28	0.12	0.10	0.10	0.12	0.20	0.21	1.04	0.30	0.03	0.00	0.00	0.00	0.00
u_{RMS}	0.27	0.43	1.57	0.32	0.21	0.05	0.04	0.04	0.05	0.09	0.23	2.44	0.16	0.11	0.00	0.00	0.00	0.00
I_A	0.55	0.39	0.71	0.43	0.36	0.31	0.43	0.38	0.36	0.28	0.18	0.65	0.47	0.25	0.24	0.19	0.19	0.23
CAV	0.50	0.46	0.92	0.20	0.30	0.53	0.34	0.38	0.48	0.15	0.24	1.66	0.07	0.90	0.06	0.03	0.03	0.06
CAD	0.29	0.46	1.58	0.22	0.68	0.17	0.10	0.11	0.15	0.07	0.24	3.37	0.06	0.97	0.03	0.02	0.02	0.03
SED	0.27	0.39	1.47	0.42	0.37	0.04	0.03	0.03	0.04	0.10	0.22	2.32	0.22	0.15	0.00	0.00	0.00	0.00
Ground motion dependent compound IMs																		
PGV/PGA	0.56	0.46	0.83	0.21	0.63	0.05	0.02	0.02	0.04	0.14	0.24	1.80	0.05	0.97	0.02	0.01	0.01	0.02
PGV^2/PGA	0.48	0.36	0.76	0.51	0.29	0.01	0.01	0.01	0.01	0.20	0.20	1.03	0.36	0.03	0.00	0.00	0.00	0.00
I_a	0.85	0.43	0.51	0.29	0.01	0.04	0.07	0.05	0.05	0.49	0.19	0.39	0.42	0.53	0.65	0.75	0.72	0.69
I_v	0.88	0.39	0.45	0.42	0.60	0.06	0.04	0.04	0.06	0.32	0.22	0.68	0.24	0.20	0.00	0.00	0.00	0.00
I_d	0.30	0.43	1.42	0.31	0.48	0.07	0.05	0.05	0.06	0.10	0.23	2.39	0.14	0.29	0.01	0.00	0.00	0.01
I_F	0.79	0.34	0.43	0.56	0.31	0.09	0.07	0.08	0.08	0.34	0.19	0.56	0.44	0.02	0.00	0.00	0.00	0.00
I_Z	−0.34	0.49	−1.46	0.08	0.00	0.30	0.46	0.40	0.34	−0.28	0.22	−0.77	0.24	0.06	0.78	0.64	0.67	0.76
I_C	0.36	0.44	1.22	0.27	0.62	0.93	0.75	0.77	0.89	0.17	0.22	1.31	0.24	0.29	0.05	0.03	0.03	0.05
SIR	0.20	0.48	2.43	0.13	0.00	0.09	0.17	0.13	0.11	0.17	0.19	1.11	0.41	0.04	0.28	0.38	0.34	0.31
Structure-independent spectral IMs																		
EPA	0.87	0.42	0.48	0.35	0.01	0.01	0.02	0.02	0.02	0.53	0.17	0.31	0.56	0.37	0.29	0.32	0.31	0.30
EPV	0.76	0.35	0.46	0.54	0.99	0.21	0.13	0.14	0.20	0.34	0.18	0.54	0.46	0.09	0.00	0.00	0.00	0.00
IEPA	0.89	0.41	0.46	0.37	0.01	0.02	0.04	0.03	0.03	0.53	0.17	0.31	0.56	0.58	0.49	0.56	0.54	0.52
IEPV	0.79	0.34	0.43	0.57	0.76	0.16	0.11	0.12	0.16	0.35	0.18	0.53	0.46	0.06	0.00	0.00	0.00	0.00
HI	0.66	0.36	0.54	0.52	0.32	0.09	0.07	0.07	0.09	0.26	0.20	0.76	0.36	0.04	0.00	0.00	0.00	0.00
ASI	0.87	0.42	0.48	0.35	0.01	0.01	0.02	0.02	0.02	0.53	0.17	0.31	0.56	0.37	0.29	0.32	0.31	0.30
ASI*	1.06	0.31	0.29	**0.65**	0.78	0.96	0.87	0.89	0.94	0.50	0.16	0.32	**0.61**	0.01	0.01	0.01	0.00	0.01
VSI	0.87	0.32	0.37	**0.61**	0.37	0.22	0.18	0.19	0.22	0.39	0.17	0.44	**0.52**	0.01	0.00	0.00	0.00	0.00
DSI	0.31	0.43	1.39	0.31	0.60	0.18	0.14	0.15	0.18	0.10	0.23	2.25	0.15	0.30	0.01	0.01	0.01	0.01
Structure-dependent spectral IMs																		
$\boldsymbol{S_a(T_1)}$	1.08	0.26	0.24	**0.75**	0.36	0.89	0.77	0.71	0.93	0.44	0.17	0.40	**0.52**	0.36	0.02	0.01	0.01	0.02
$S_a(T_2)$	0.88	0.37	0.43	0.47	0.04	0.25	0.35	0.35	0.25	0.40	0.19	0.49	0.41	0.89	0.27	0.22	0.19	0.30
$S_a(T_3)$	0.80	0.39	0.49	0.42	0.10	0.26	0.34	0.32	0.29	0.41	0.18	0.45	0.47	0.73	0.29	0.26	0.24	0.29
$S_a(T_4)$	0.74	0.42	0.57	0.33	0.04	0.13	0.18	0.16	0.16	0.42	0.19	0.45	0.43	0.92	0.72	0.66	0.66	0.69
$S_a(T_5)$	0.74	0.42	0.57	0.33	0.04	0.13	0.18	0.16	0.16	0.42	0.19	0.45	0.43	0.92	0.72	0.66	0.66	0.69
$S_a(T_6)$	0.74	0.42	0.57	0.33	0.04	0.13	0.18	0.16	0.16	0.42	0.19	0.45	0.43	0.92	0.72	0.66	0.66	0.69
$S_a(T_7)$	0.74	0.42	0.57	0.33	0.04	0.13	0.18	0.16	0.16	0.42	0.19	0.45	0.43	0.92	0.72	0.66	0.66	0.69
$S_a(T_8)$	0.74	0.42	0.57	0.33	0.04	0.13	0.18	0.16	0.16	0.42	0.19	0.45	0.43	0.92	0.72	0.66	0.66	0.69

(*continued on next page*)

Table A2 (*continued*)

EDP	$\max(\overline{\Delta_r})$									$\max(V_b)$								
IM	*b*	$\beta_{EDP\|IM}$	ζ	R^2	*p-value*					*b*	$\beta_{EDP\|IM}$	ζ	R^2	*p-value*				
					M_w	R_{epi}	R_{rup}	R_{JB}	R_{hyp}					M_w	R_{epi}	R_{rup}	R_{JB}	R_{hyp}
$S_a(T_9)$	0.74	0.42	0.57	0.33	0.04	0.13	0.18	0.16	0.16	0.42	0.19	0.45	0.43	0.92	0.72	0.66	0.66	0.69
$S_a(T_{10})$	0.57	0.45	0.80	0.23	0.01	0.16	0.26	0.21	0.20	0.36	0.20	0.55	0.38	0.36	0.84	0.70	0.73	0.78
$\boldsymbol{S_v(T_1)}$	1.18	0.27	0.23	**0.72**	0.20	0.58	0.67	0.70	0.57	0.51	0.16	0.31	**0.59**	0.36	0.03	0.03	0.02	0.04
$S_v(T_2)$	0.81	0.41	0.50	0.38	0.02	0.13	0.20	0.19	0.15	0.40	0.20	0.49	0.39	0.64	0.56	0.47	0.44	0.58
$S_v(T_3)$	0.70	0.43	0.61	0.31	0.04	0.18	0.26	0.23	0.22	0.40	0.19	0.48	0.42	0.84	0.56	0.50	0.50	0.55
$S_v(T_4)$	0.58	0.46	0.79	0.21	0.02	0.12	0.19	0.16	0.15	0.36	0.20	0.56	0.35	0.50	0.99	0.89	0.92	0.96
$S_v(T_5)$	0.58	0.46	0.79	0.21	0.02	0.12	0.19	0.16	0.15	0.36	0.20	0.56	0.35	0.50	0.99	0.89	0.92	0.96
$S_v(T_6)$	0.58	0.46	0.79	0.21	0.02	0.12	0.19	0.16	0.15	0.36	0.20	0.56	0.35	0.50	0.99	0.89	0.92	0.96
$S_v(T_7)$	0.58	0.46	0.79	0.21	0.02	0.12	0.19	0.16	0.15	0.36	0.20	0.56	0.35	0.50	0.99	0.89	0.92	0.96
$S_v(T_8)$	0.58	0.46	0.79	0.21	0.02	0.12	0.19	0.16	0.15	0.36	0.20	0.56	0.35	0.50	0.99	0.89	0.92	0.96
$S_v(T_9)$	0.58	0.46	0.79	0.21	0.02	0.12	0.19	0.16	0.15	0.36	0.20	0.56	0.35	0.50	0.99	0.89	0.92	0.96
$S_v(T_{10})$	0.41	0.48	1.17	0.13	0.01	0.20	0.33	0.28	0.25	0.29	0.21	0.73	0.28	0.27	0.89	0.73	0.77	0.84
$\boldsymbol{S_d(T_1)}$	1.08	0.26	0.24	**0.75**	0.36	0.87	0.75	0.70	0.91	0.43	0.17	0.40	**0.52**	0.36	0.02	0.01	0.01	0.02
$S_d(T_2)$	0.88	0.37	0.43	0.47	0.04	0.26	0.35	0.36	0.26	0.40	0.19	0.49	0.41	0.89	0.27	0.22	0.18	0.30
$S_d(T_3)$	0.80	0.39	0.49	0.42	0.10	0.27	0.34	0.32	0.30	0.41	0.18	0.45	0.46	0.73	0.28	0.26	0.24	0.29
$S_d(T_4)$	0.75	0.42	0.57	0.33	0.04	0.13	0.18	0.16	0.16	0.42	0.19	0.45	0.43	0.93	0.71	0.66	0.66	0.69
$S_d(T_5)$	0.75	0.42	0.57	0.33	0.04	0.13	0.18	0.16	0.16	0.42	0.19	0.45	0.43	0.93	0.71	0.66	0.66	0.69
$S_d(T_6)$	0.75	0.42	0.57	0.33	0.04	0.13	0.18	0.16	0.16	0.42	0.19	0.45	0.43	0.93	0.71	0.66	0.66	0.69
$S_d(T_7)$	0.75	0.42	0.57	0.33	0.04	0.13	0.18	0.16	0.16	0.42	0.19	0.45	0.43	0.93	0.71	0.66	0.66	0.69
$S_d(T_8)$	0.75	0.42	0.57	0.33	0.04	0.13	0.18	0.16	0.16	0.42	0.19	0.45	0.43	0.93	0.71	0.66	0.66	0.69
$S_d(T_9)$	0.75	0.42	0.57	0.33	0.04	0.13	0.18	0.16	0.16	0.42	0.19	0.45	0.43	0.93	0.71	0.66	0.66	0.69
$S_d(T_{10})$	0.57	0.45	0.80	0.23	0.01	0.16	0.26	0.21	0.20	0.36	0.20	0.55	0.38	0.36	0.84	0.69	0.73	0.78
$S_a(T = 0.1\ s)$	0.13	0.51	3.82	0.02	0.00	0.24	0.40	0.35	0.28	0.18	0.23	1.28	0.18	0.04	0.39	0.53	0.49	0.42
$S_a(T = 0.2\ s)$	0.38	0.48	1.27	0.12	0.01	0.13	0.22	0.19	0.16	0.30	0.21	0.71	0.30	0.17	0.66	0.81	0.79	0.70
$S_a(T = 0.5\ s)$	1.08	0.26	0.24	0.75	0.36	0.89	0.77	0.71	0.93	0.44	0.17	0.40	0.52	0.36	0.02	0.01	0.01	0.02
$S_a(T = 1.0\ s)$	0.50	0.39	0.78	0.41	0.76	0.24	0.14	0.15	0.23	0.21	0.21	1.03	0.29	0.32	0.00	0.00	0.00	0.01
$\boldsymbol{S_a}^*$	0.83	0.31	0.38	**0.63**	0.79	0.15	0.10	0.10	0.16	0.34	0.19	0.55	**0.44**	0.12	0.00	0.00	0.00	0.00
$\overline{S_a}$	0.99	0.27	0.27	**0.73**	0.44	0.11	0.08	0.07	0.12	0.40	0.18	0.44	**0.50**	0.05	0.00	0.00	0.00	0.00
$\overline{\overline{S_a}}$	0.82	0.32	0.39	**0.62**	0.60	0.11	0.07	0.07	0.11	0.33	0.19	0.57	**0.43**	0.08	0.00	0.00	0.00	0.00
$S_a^{1\text{-}to\text{-}2}$	0.91	0.37	0.40	0.50	0.04	0.26	0.35	0.36	0.26	0.41	0.19	0.47	0.42	0.95	0.25	0.20	0.17	0.28
$S_a^{1\text{-}to\text{-}3}$	0.91	0.37	0.40	0.50	0.04	0.26	0.35	0.36	0.26	0.41	0.19	0.47	0.42	0.95	0.25	0.20	0.17	0.28
$S_a^{1\text{-}to\text{-}4}$	0.91	0.37	0.40	0.50	0.04	0.25	0.34	0.34	0.25	0.41	0.19	0.46	0.43	0.96	0.26	0.21	0.18	0.29
$S_a^{1\text{-}to\text{-}5}$	0.91	0.37	0.40	0.50	0.05	0.25	0.33	0.34	0.25	0.41	0.19	0.46	0.43	0.96	0.26	0.21	0.18	0.29
$S_a^{1\text{-}to\text{-}6}$	0.91	0.37	0.40	0.50	0.05	0.25	0.33	0.34	0.25	0.41	0.19	0.46	0.43	0.96	0.26	0.21	0.18	0.29
$S_a^{1\text{-}to\text{-}7}$	0.91	0.37	0.40	0.50	0.05	0.25	0.33	0.34	0.25	0.41	0.19	0.46	0.43	0.96	0.26	0.21	0.18	0.29
$S_a^{1\text{-}to\text{-}8}$	0.91	0.37	0.40	0.50	0.05	0.25	0.33	0.34	0.25	0.41	0.19	0.46	0.43	0.96	0.26	0.21	0.18	0.29
$S_a^{1\text{-}to\text{-}9}$	0.92	0.37	0.40	0.50	0.05	0.24	0.33	0.34	0.24	0.41	0.19	0.45	0.43	0.97	0.26	0.22	0.18	0.30
$S_a^{1\text{-}to\text{-}10}$	0.94	0.36	0.39	0.50	0.04	0.20	0.27	0.28	0.20	0.43	0.19	0.43	0.45	0.97	0.30	0.25	0.22	0.34

References

[1] Naeim F, Bhatia H, Lobo RM. Performance based seismic engineering. The seismic design handbook. 2001. p. 757–92.

[2] Kramer SL. Performance-based earthquake engineering: opportunities and implications for geotechnical engineering practice. Geotechnical earthquake engineering and soil dynamics IV. 2008. p. 1–32.

[3] Porter K, Kennedy R, Bachman R. Creating fragility functions for performance-based earthquake engineering. Earthq Spectra 2007;23:471–89.

[4] Faggella M, Barbosa AR, Conte JP, Spacone E, Restrepo JI. Probabilistic seismic response analysis of a 3-D reinforced concrete building. Struct Saf 2013;44:11–27.

[5] Gencturk B, Hossain K, Lahourpour S. Life cycle sustainability assessment of RC buildings in seismic regions. Eng Struct 2016;110:347–62.

[6] Terzic V, Mahin SA. Using PBEE to assess and improve performance of different structural systems for low-rise steel buildings 2017.

[7] Mackie KR, Stojadinović B. Performance-based seismic bridge design for damage and loss limit states. Earthq Eng Struct Dyn 2007;36:1953–71.

[8] Mackie KR, Lu J, Elgamal A. Performance-based earthquake assessment of bridge systems including ground-foundation interaction. Soil Dyn Earthq Eng 2012;42:184–96.

[9] Roca P, Cervera M, Gariup G, Pela' L. Structural analysis of masonry historical constructions. Classical and advanced approaches. Arch Comput Methods Eng 2010;17. https://doi.org/10.1007/s11831-010-9046-1.

[10] D'Altri AM, Sarhosis V, Milani G, Rots J, Cattari S, Lagomarsino S, et al. Modeling strategies for the computational analysis of unreinforced masonry structures: review and classification. Arch Comput Methods Eng 2020;27. https://doi.org/10.1007/s11831-019-09351-x.

[11] Tomić I, Vanin F, Beyer K. Uncertainties in the seismic assessment of historical masonry buildings. Appl Sci 2021;11:2280.

[12] Parisse F, Cattari S, Marques R, Lourenço PB, Magenes G, Beyer K, et al. Benchmarking the seismic assessment of unreinforced masonry buildings from a blind prediction test. Structures 2021;31. https://doi.org/10.1016/j.istruc.2021.01.096.

[13] Cattari S, Magenes G. Benchmarking the software packages to model and assess the seismic response of unreinforced masonry existing buildings through nonlinear static analyses. Bull Earthq Eng 2022;20. https://doi.org/10.1007/s10518-021-01078-0.

[14] Tomić I, Penna A, DeJong M, Butenweg C, Correia AA, Candeias PX, et al. Shake-table testing of a stone masonry building aggregate: overview of blind prediction study. Bull Earthq Eng 2023. https://doi.org/10.1007/s10518-022-01582-x.

[15] Lagomarsino S, Cattari S. PERPETUATE guidelines for seismic performance-based assessment of cultural heritage masonry structures. Bull Earthq Eng 2015;13:13–47.

[16] Park J, Towashiraporn P, Craig JI, Goodno BJ. Seismic fragility analysis of low-rise unreinforced masonry structures. Eng Struct 2009;31:125–37.

[17] Standard B. Eurocode 6—Design of masonry structures. London: British Standard Institution; 2005.

[18] Donà M, Morandi P, Minotto M, Manzini CF, da Porto F, Magenes G. Second-order effects in URM walls subjected to compression and out-of-plane bending: from numerical evaluation to proposal of design procedures. Eng Struct 2020;209. https://doi.org/10.1016/j.engstruct.2019.110130.

[19] Morandi P, Magenes G, Griffith M. Second order effects in out-of-plane strength of unreinforced masonry walls subjected to bending and compression. Austral J Struct Eng 2008;8. https://doi.org/10.1080/13287982.2008.11464993.

[20] Donà M, Tecchio G, da Porto F. Verification of second-order effects in slender reinforced masonry walls. Mater Struct 2018;51. https://doi.org/10.1617/s11527-018-1196-x.

[21] Karimzadeh S, Kadaş K, Askan A, Erberik MA, Yakut A. A study on fragility analyses of masonry buildings in Erzincan (Turkey) utilizing simulated and real ground motion records. Procedia Eng 2017;199:188–93.

[22] Karimzadeh S, Kadasa K, Askanb A, Erberikb MA, Yakutb A. Derivation of analytical fragility curves using SDOF models of masonry structures in Erzincan (Turkey). Earthq Struct 2020;18. https://doi.org/10.12989/eas.2020.18.2.249.

[23] Koc AB, Erberik MA, Askan A, Karimzadeh S. The sensitivity of global structural parameters for unreinforced masonry buildings subjected to simulated ground motions. Buildings 2023;13. https://doi.org/10.3390/buildings13082060.
[24] Karimzadeh S, Funari MF, Szabó S, Hussaini SMS, Rezaeian S, Lourenço PB. Stochastic simulation of earthquake ground motions for the seismic assessment of monumental masonry structures: source-based vs site-based approaches. Earthq Eng Struct Dyn 2023. https://doi.org/10.1002/eqe.4012.
[25] Battaglia L, Ferreira TM, Lourenço PB. Seismic fragility assessment of masonry building aggregates: a case study in the old city centre of Seixal, Portugal. Earthq Eng Struct Dyn 2021;50:1358–77.
[26] Angiolilli M, Lagomarsino S, Cattari S, Degli Abbati S. Seismic fragility assessment of existing masonry buildings in aggregate. Eng Struct 2021;247:113218.
[27] Tomić I, Beyer K. Shake-table test on a historical masonry aggregate: prediction and postdiction using an equivalent-frame model. Bull Earthq Eng 2023. https://doi.org/10.1007/s10518-023-01765-0.
[28] Xu Y, Lu X, Tian Y, Huang Y. Real-time seismic damage prediction and comparison of various ground motion intensity measures based on machine learning. J Earthq Eng 2022;26:4259–79.
[29] Rosti A, Rota M, Penna A. Empirical fragility curves for Italian URM buildings. Bull Earthq Eng 2021;19:3057–76.
[30] Faravelli M, Polli D, Quaroni D, Onida M, Pagano M, Di Meo A, et al. Italian platform for seismic risk and damage scenario evaluation. In: 7th international conference on computational methods in structural dynamics and earthquake engineering COMPDYN; 2019.
[31] Lagomarsino S, Cattari S, Ottonelli D. The heuristic vulnerability model: fragility curves for masonry buildings. Bull Earthq Eng 2021;19:3129–63.
[32] Lagomarsino S, Giovinazzi S. Macroseismic and mechanical models for the vulnerability and damage assessment of current buildings. Bull Earthq Eng 2006;4:415–43.
[33] da Porto F, Donà M, Rosti A, Rota M, Lagomarsino S, Cattari S, et al. Comparative analysis of the fragility curves for Italian residential masonry and RC buildings. Bull Earthq Eng 2021;19:3209–52.
[34] Donà M, Carpanese P, Follador V, Sbrogiò L, da Porto F. Mechanics-based fragility curves for Italian residential URM buildings. Bull Earthq Eng 2021;19:3099–127.
[35] Saler E, Follador V, Carpanese P, Donà M, da Porto F. Development of mechanics-based fragility curves for the Italian masonry school asset. Earthq Spectra 2024:87552930241245730.
[36] Monti G, Rabi RR, Demartino C. Spectrum-consistent ag-based fragility curves. Reliab Eng Syst Saf 2024;245:109977.
[37] Xiao-hui YU, Guang-yuan W. Discussions on probabilistic seismic demand models. 工程力学 2013;30:172–9.
[38] Cornell CA, Jalayer F, Hamburger RO, Foutch DA. Probabilistic basis for 2000 SAC federal emergency management agency steel moment frame guidelines. J Struct Eng 2002;128:526–33.
[39] Mitropoulou CC, Papadrakakis M. Developing fragility curves based on neural network IDA predictions. Eng Struct 2011;33:3409–21.
[40] Wang Z, Pedroni N, Zentner I, Zio E. Seismic fragility analysis with artificial neural networks: application to nuclear power plant equipment. Eng Struct 2018;162:213–25.
[41] Quinci G, Paolacci F, Fragiadakis M, Bursi OS. A machine learning framework for seismic risk assessment of industrial equipment. Reliab Eng Syst Saf 2025;254:110606.
[42] Barroso LR, Winterstein S. Probabilistic seismic demand analysis of controlled steel moment-resisting frame structures. Earthq Eng Struct Dyn 2002;31:2049–66.
[43] Freddi F, Padgett JE, Dall'Asta A. Probabilistic seismic demand modeling of local level response parameters of an RC frame. Bull Earthq Eng 2017;15:1–23.
[44] Mackie K, Stojadinović B. Probabilistic seismic demand model for California highway bridges. J Bridge Eng 2001;6:468–81.
[45] Tondini N, Stojadinovic B. Probabilistic seismic demand model for curved reinforced concrete bridges. Bull Earthq Eng 2012;10:1455–79.
[46] Hariri-Ardebili MA, Saouma VE. Probabilistic seismic demand model and optimal intensity measure for concrete dams. Struct Safety 2016;59:67–85.
[47] Tian L, Pan H, Ma R. Probabilistic seismic demand model and fragility analysis of transmission tower subjected to near-field ground motions. J Constr Steel Res 2019;156:266–75.
[48] Liu J, Tian L, Yang M, Meng X. Probabilistic framework for seismic resilience assessment of transmission tower-line systems subjected to mainshock-aftershock sequences. Reliab Eng Syst Saf 2024;242:109755.
[49] Heshmati M, Jahangiri V. Appropriate intensity measures for probabilistic seismic demand estimation of steel diagrid systems. Eng Struct 2021;249:113260.
[50] Zhao Y-G, Qin M-J, Lu Z-H, Zhang L-W. Seismic fragility analysis of nuclear power plants considering structural parameter uncertainty. Reliab Eng Syst Saf 2021;216:107970.
[51] Zhou L, Alam MS, Wang X, Ye A, Zhang P. Optimal intensity measure selection and probabilistic seismic demand model of pile group supported bridges in sandy soil considering variable scour effects. Ocean Eng 2023;285:115365.
[52] Che W, Chang P, Wang W. Optimal intensity measures for probabilistic seismic stability assessment of large open-pit mine slopes under different mining depths. Shock Vib 2023. 2023.
[53] Khalid MI, Park D, Fei J, Nguyen V-Q, Nguyen D-D, Chen X. Selection of efficient earthquake intensity measures for evaluating seismic fragility of concrete face rockfill dam. Comput Geotech 2023;163:105721.
[54] Liu X, Xie Q. A probabilistic framework to evaluate seismic resilience of substations based on three-stage uncertainty. Reliab Eng Syst Saf 2024;249:110219.
[55] Hariri-Ardebili MA, Rezaeian S. Utilization of stochastic ground motion simulations for scenario-based performance assessment of geo-structures. Reliab Eng Syst Saf 2024;251:110375.
[56] Zhang Q, Zhao Y-G, Kolozvari K, Xu L. Reliability analysis of reinforced concrete structure against progressive collapse. Reliab Eng Syst Saf 2022;228:108831.
[57] Zhou Z, Yu X, Gardoni P, Ji K, Lu D. Seismic risk estimates for reinforced concrete structures with incorporation of corrosion and aftershock. Reliab Eng Syst Saf 2025;254:110585.
[58] Vargas-Alzate YF, Hurtado JE. Efficiency of intensity measures considering near- and far-fault ground motion records. Geosciences 2021;11:234.
[59] Guo J, Alam MS, Wang J, Li S, Yuan W. Optimal intensity measures for probabilistic seismic demand models of a cable-stayed bridge based on generalized linear regression models. Soil Dyn Earthq Eng 2020;131:106024.
[60] Tibshirani R. Regression shrinkage and selection via the lasso. J R Stat Soc Series B 1996;58:267–88.
[61] McKenna F. OpenSees: a framework for earthquake engineering simulation. Comput Sci Eng 2011;13:58–66.
[62] Vanin F, Penna A, Beyer K. A three-dimensional macroelement for modelling the in-plane and out-of-plane response of masonry walls. Earthq Eng Struct Dyn 2020;49. https://doi.org/10.1002/eqe.3277.
[63] Bernardo V, Karimzadeh S, Caicedo D, Hussaini SMS, Lourenço PB. Fragility-based seismic assessment of traditional masonry buildings on Azores (Portugal) using simulated ground-motion records. Earthq Spectra 2024;40:2836–61.
[64] Chiozzi A, Milani G, Grillanda N, Tralli A. A fast and general upper-bound limit analysis approach for out-of-plane loaded masonry walls. Meccanica 2018;53:1875–98.
[65] Jayaram N, Lin T, Baker JW. A computationally efficient ground-motion selection algorithm for matching a target response spectrum mean and variance. Earthq Spectra 2011;27. https://doi.org/10.1193/1.3608002.
[66] Michel C, Karbassi A, Lestuzzi P. Evaluation of the seismic retrofitting of an unreinforced masonry building using numerical modeling and ambient vibration measurements. Eng Struct 2018;158:124–35.
[67] da Silva LCM, Milani G. A FE-based macro-element for the assessment of masonry structures: linear static, vibration, and non-linear cyclic analyses. Appl Sci 2022;12. https://doi.org/10.3390/app12031248.
[68] Funari MF, Silva LC, Savalle N, Lourenço PB. A concurrent Micro/Macro FE-model optimized with A limit analysis tool for the assessment of dry-joint masonry structures. Int J Multiscale Comput Eng 2022;20. https://doi.org/10.1615/IntJMultCompEng.2021040212.
[69] Pulatsu B, Bretas EM, Lourenço PB. Discrete element modeling of masonry structures: validation and application. Earthq Struct 2016;11. https://doi.org/10.12989/eas.2016.11.4.563.
[70] Funari MF, Pulatsu B, Szabó S, Lourenço PB. A solution for the frictional resistance in macro-block limit analysis of non-periodic masonry. Structures 2022;43. https://doi.org/10.1016/j.istruc.2022.06.072.
[71] Quagliarini E, Maracchini G, Clementi F. Uses and limits of the Equivalent Frame Model on existing unreinforced masonry buildings for assessing their seismic risk: a review. J Build Eng 2017;10:166–82.
[72] Vanin F, Penna A, Beyer K. Equivalent-frame modeling of two shaking table tests of masonry buildings accounting for their out-of-plane response. Front Built Environ 2020;6. https://doi.org/10.3389/fbuil.2020.00042.
[73] Tomić I, Vanin F, Božulić I, Beyer K. Numerical simulation of unreinforced masonry buildings with timber diaphragms. Buildings 2021;11. https://doi.org/10.3390/buildings11050205.
[74] Nale M, Minghini F, Chiozzi A, Tralli A. Fragility functions for local failure mechanisms in unreinforced masonry buildings: a typological study in Ferrara, Italy. Bull Earthq Eng 2021;19. https://doi.org/10.1007/s10518-021-01199-6.
[75] Penna A, Lagomarsino S, Galasco A. A nonlinear macroelement model for the seismic analysis of masonry buildings. Earthq Eng Struct Dyn 2014;43. https://doi.org/10.1002/eqe.2335.
[76] Guerrini G., Senaldi I., Scherini S., Morganti S., Magenes G. Material characterization for the shaking-table test of the scaled prototype of a stone masonry building aggregate. 2017:105–15.
[77] Senaldi I, Guerrini G, Scherini S, Morganti S, Magenes G, Beyer K, et al. Natural stone masonry characterization for the shaking-table test of a scaled building specimen. In: Proceedings of the international masonry society conferences. 0; 2018.
[78] Guerrini G, Senaldi I, Graziotti F, Magenes G, Beyer K, Penna A. Shake-table test of a strengthened stone masonry building aggregate with flexible diaphragms. Int J Architect Heritage 2019;13. https://doi.org/10.1080/15583058.2019.1635661.
[79] Brignola A, Podestà S, Pampanin S. In-plane stiffness of wooden floor. In: 2008 NZSEE Conference. 49; 2008. Paper.
[80] Brignola A, Pampanin S, Podestà S. Experimental evaluation of the in-plane stiffness of timber diaphragms. Earthq Spectra 2012;28:1687–709.
[81] POLIMI. Critical review of methodologies and tools for assessment of failure mechanisms and interventions. Deliverable 3.3, Workpackage 3: Damage Based Selection Of Technologies; 2010.
[82] Almeida JP, Beyer K, Brunner R, Wenk T. Characterization of mortar–timber and timber–timber cyclic friction in timber floor connections of masonry buildings. Mater Struct 2020;53. https://doi.org/10.1617/s11527-020-01483-y.
[83] Vanin F, Zaganelli D, Penna A, Beyer K. Estimates for the stiffness, strength and drift capacity of stone masonry walls based on 123 quasi-static cyclic tests

reported in the literature. Bull Earthq Eng 2017;15. https://doi.org/10.1007/s10518-017-0188-5.
[84] Salvalaggio M, Bernardo V, Lourenço PB. Exploring seismic fragility and strengthening of masonry built heritage in Lisbon (Portugal) via the Applied Element Method. Eng Struct 2024;320:118890.
[85] Akkar S, Sandıkkaya MA, Şenyurt M, Sisi AA, Ay B, Traversa P, et al. Reference database for seismic ground-motion in Europe (RESORCE). Bull Earthq Eng 2014;12. https://doi.org/10.1007/s10518-013-9506-8.
[86] Lanzano G, Sgobba S, Luzi L, Puglia R, Pacor F, Felicetta C, et al. The pan-European Engineering Strong Motion (ESM) flatfile: compilation criteria and data statistics. Bull Earthq Eng 2019;17:561–82.
[87] Disaster, Authority EM. Turkish National Strong Motion Network 1973. https://doi.org/10.7914/SN/TK.
[88] Luzi L, Hailemikael S, Bindi D, Pacor F, Mele F, Sabetta F. ITACA (ITalian ACcelerometric Archive): a web portal for the dissemination of the Italian strong motion data. Seismol Res Lett 2008.
[89] Trifunac MD, Brady AG. A study on the duration of strong earthquake ground motion. Bull Seismol Soc Am 1978:65.
[90] Rathje EM, Abrahamson NA, Bray JD. Simplified frequency content estimates of earthquake ground motions. J Geotech Geoenviron Eng 1998;124. https://doi.org/10.1061/(asce)1090-0241(1998)124:2(150).
[91] Housner GW. Measures of severity of earthquake ground shaking. In: Proceedings of US national conference on earthquake engineering. 6; 1975. p. 1975.
[92] Arias A. A measure of earthquake intensity. Seismic design for nuclear power plants. 1970.
[93] Reed JW, Kassawara RP. A criterion for determining exceedance of the operating basis earthquake. Nucl Eng Des 1990;123. https://doi.org/10.1016/0029-5493(90)90259-Z.
[94] Riddell R, Garcia JE. Hysteretic energy spectrum and damage control. Earthq Eng Struct Dyn 2001;30:1791–816.
[95] Fajfar P, Vidic T, Fischinger M. A measure of earthquake motion capacity to damage medium-period structures. Soil Dyn Earthq Eng 1990;9. https://doi.org/10.1016/S0267-7261(05)80002-8.
[96] Cosenza E, Manfredi G. A seismic design method including damage effect. In: 11th European conference on earthquake engineering; 1998. p. 6–11.
[97] Park Y, Ang AH -S, Wen YK. Seismic damage analysis of reinforced concrete buildings. J Struct Eng 1985;111. https://doi.org/10.1061/(asce)0733-9445(1985)111:4(740).
[98] Dashti S, Bray JD, Pestana JM, Riemer M, Wilson D. Centrifuge testing to evaluate and mitigate liquefaction-induced building settlement mechanisms. J Geotech Geoenviron Eng 2010;136:918–29.
[99] Council AT, of California SEA. Tentative provisions for the development of seismic regulations for buildings: a cooperative effort with the design professions, building code interests, and the research community. Department of Commerce, National Bureau of Standards; 1978.
[100] Yang D, Pan J, Li G. Non-structure-specific intensity measure parameters and characteristic period of near-fault ground motions. Earthq Eng Struct Dyn 2009;38:1257–80.
[101] Housner GW. Intensity of ground motion during strong earthquakes. 1952.
[102] von Thun JL, Roehm LH, Scott GA, Wilson JA. Earthquake ground motions for design and analysis of dams. Earthquake engineering and soil dynamics II - recent advances in ground-motion evaluation. In: Proceedings of the specialty conference; 1988.
[103] Yakut A, Yılmaz H. Correlation of deformation demands with ground motion intensity. J Struct Eng 2008;134:1818–28.
[104] Cordova PP, Deierlein GG, Mehanny SSF, Cornell CA. Development of a two-parameter seismic intensity measure and probabilistic assessment procedure. In: The second US-Japan workshop on performance-based earthquake engineering methodology for reinforced concrete building structures. 20; 2000. p. 0.
[105] Vamvatsikos D, Cornell CA. Developing efficient scalar and vector intensity measures for IDA capacity estimation by incorporating elastic spectral shape information. Earthq Eng Struct Dyn 2005;34:1573–600.
[106] Zhou Y, Su N, Lu X. An elastic spectral value-based intensity measure for the incremental dynamic analysis of tall buildings. In: Proceedings of the 5th Kwang-Hua Forum on innovations and implementations in earthquake engineering research; 2012.
[107] Shome N, Cornell CA, Bazzurro P, Carballo JE. Earthquakes, records, and nonlinear responses. Earthq Spectra 1998;14:469–500.
[108] Tothong P, Luco N. Probabilistic seismic demand analysis using advanced ground motion intensity measures. Earthq Eng Struct Dyn 2007;36:1837–60.
[109] Padgett JE, Nielson BG, DesRoches R. Selection of optimal intensity measures in probabilistic seismic demand models of highway bridge portfolios. Earthq Eng Struct Dyn 2008;37:711–25.
[110] Giovenale P, Cornell CA, Esteva L. Comparing the adequacy of alternative ground motion intensity measures for the estimation of structural responses. Earthq Eng Struct Dyn 2004;33:951–79.
[111] Mohammadi A, Karimzadeh S, Banimahd SA, Ozsarac V, Lourenço PB. The potential of region-specific machine-learning-based ground motion models: application to Turkey. Soil Dyn Earthq Eng 2023;172:108008.
[112] Karimzadeh S, Mohammadi A, Hussaini SMS, Caicedo D, Askan A, Lourenço PB. ANN-based ground motion model for Turkey using stochastic simulation of earthquakes. Geophys J Int 2023:ggad432.
[113] Shao J. Linear model selection by cross-validation. J Am Stat Assoc 1993;88:486–94.
[114] Vamvatsikos D, Cornell CA. Incremental dynamic analysis. Earthq Eng Struct Dyn 2002;31:491–514.
[115] Ni PP, Wang SH, Jiang L, Huang RQ. Seismic risk assessment of structures using multiple stripe analysis. Appl Mech Mater 2012;226:897–900.
[116] Caicedo D, Tomić I, Karimzadeh S, Bernardo V, Beyer K, Lourenço PB. Collapse fragility analysis of historical masonry buildings considering in-plane and out-of-plane response of masonry walls. Eng Struct 2024;319:118804.
[117] Akkar S, Sandıkkaya MA, Bommer JJ. Empirical ground-motion models for point- and extended-source crustal earthquake scenarios in Europe and the Middle East. Bull Earthq Eng 2014;12:359–87.
[118] Bindi D, Cotton F, Kotha SR, Bosse C, Stromeyer D, Grünthal G. Application-driven ground motion prediction equation for seismic hazard assessments in non-cratonic moderate-seismicity areas. J Seismol 2017;21:1201–18.
[119] Kotha SR, Weatherill G, Bindi D, Cotton F. A regionally-adaptable ground-motion model for shallow crustal earthquakes in Europe. Bull Earthq Eng 2020;18:4091–125.
[120] Chopra AK. Dynamics of structures. Pearson Education India; 2007.
[121] Banimahd SA, Giouvanidis AI, Karimzadeh S, Lourenço PB. A multi-level approach to predict the seismic response of rigid rocking structures using artificial neural networks. Earthq Eng Struct Dyn 2024;53:2185–208.
[122] Giouvanidis A., Karimzadeh S., Banimahd A., Lourenço P.B. Investigating the interaction between rocking amplitude and ground motion characteristics via artificial neural networks 2024.
[123] Costa AA, Penna A, Arêde A, Costa A. Simulation of masonry out-of-plane failure modes by multi-body dynamics. Earthq Eng Struct Dyn 2015;44. https://doi.org/10.1002/eqe.2596.
[124] De Felice G, Giannini R. Out-of-plane seismic resistance of masonry walls. J Earthq Eng 2001;5. https://doi.org/10.1080/13632460109350394.
[125] Aşıkoğlu A, Vasconcelos G, Lourenço PB, Pantò B. Pushover analysis of unreinforced irregular masonry buildings: lessons from different modeling approaches. Eng Struct 2020;218. https://doi.org/10.1016/j.engstruct.2020.110830.
[126] Aşıkoğlu A, Avşar Ö. Investigation of drift-based damage limit states for historical masonry structures. Int J Architect Heritage 2023;17. https://doi.org/10.1080/15583058.2022.2053612.
[127] Kocaman İ, Kazaz İ. Global drift ratio limits for historical masonry mosques. Bull Earthq Eng 2023;21. https://doi.org/10.1007/s10518-023-01613-1.
[128] Donà M, Piredda G, Zonta A, Bernardi E, da Porto F. Seismic fragility of unbraced industrial steel pallet racks. Struct Saf 2024;110:102497.
[129] Manfredi V, Masi A, Nicodemo G, Digrisolo A. Seismic fragility curves for the Italian RC residential buildings based on non-linear dynamic analyses. Bull Earthq Eng 2023;21. https://doi.org/10.1007/s10518-022-01605-7.